24

IS-T--1834

Processing of R-Ba-Cu-O Superconductors

by

Wu, Hengning

PHD Thesis submitted to Iowa State University

Ames Laboratory, U.S. DOE
Iowa State University
Ames, Iowa 50011

Date Transmitted: February 23, 1998

PREPARED FOR THE U.S. DEPARTMENT OF ENERGY
UNDER CONTRACT NO. W-7405-Eng-82.

DISCLAIMER

To Wei

TABLE OF CONTENTS

ABSTRACT

Precipitation processes were developed to introduce second phases as flux pinning centers in Gd-Ba-Cu-O and Nd-Ba-Cu-O superconductors. In Gd-Ba-Cu-O, precipitation is caused by the decrease of the upper solubility limit of $Gd_{1+x}Ba_{2-x}Cu_3O_7$ solid solution (Gd123ss) in low oxygen partial pressure. Processing of supersaturated $Gd_{1.2}Ba_{1.8}Cu_3O_7$ in low oxygen partial pressure can produce dispersed second phases. Gd211 is formed as a separate phase while extensive Gd124-type stacking fault is formed instead of a separate CuO phase. As a result of the precipitation reaction, the transition temperature and critical current density are increased. In Nd-Ba-Cu-O, precipitation is caused by the decrease of the lower solubility limit of $Nd_{1+x}Ba_{2-x}Cu_3O_7$ solid solution (Nd123ss) in oxygen. DTA results reveal the relative stability of Nd123ss in different oxygen partial pressures. In 1 bar oxygen partial pressure, Nd123ss with $x = 0.1$ is the most stable phase. In lower oxygen partial pressures, the most stable composition shifts towards the stoichiometric composition. The relative stability changes faster with decreasing oxygen partial pressure. Therefore, processing in oxygen and air tends to produce broad superconducting transitions but sharp transitions can be achieved in 0.01 bar and 0.001 bar oxygen partial pressures. While the lower solubility limits in 0.01 bar and 0.001 bar oxygen partial pressures remain at $x = 0.00$, the solubility limits in oxygen and air show a narrowing with decreasing temperature. Because of the narrowing of the solubility range in oxygen, oxygen annealing of Nd123 initially processed in low oxygen partial pressures will result in precipitation of second phases. The equilibrium second phase is $BaCuO_2$ for temperature above 608°C, and at lower temperatures the equilibrium second phases are

$Ba_2CuO_{3.3}$ and $Ba_2Cu_3O_{5+y}$. However, annealing at low temperature may produce a fine metastable transition phase. A coherent intermediate perovskite structure with a composition of $BaCuO_2$ is observed along with a high density of dislocations during the precipitation process at 500°C in oxygen. It is believed that oxygen annealing at 900°C produces the equilibrium $BaCuO_2$ phase. These precipitates are responsible for the strong flux pinning in Nd123 melt-textured in low oxygen partial pressure.

CHAPTER I INTRODUCTION

The practical application of bulk high T_c superconductors depends on the development of processing and fabrication methods to achieve high critical current density (J_c) in a magnetic field in a useful form. For commercial application in high field magnets, energy storage devices, motors and generators, and power transmission cables, they need to be manufactured into composite multifilamentary wires with a metal substrate. Among the three major types of high T_c materials, R-Ba-Cu-O, Bi-Sr-Ca-Cu-O and Tl-Ba-Ca-Cu-O (the compounds will be labeled by the first element and the cation ratio in the given order and R represents Y and rare earth elements), only Bi2212 and Bi2223 superconductors have been fabricated by the powder-in-tube method with high J_c in a high magnetic field.[1,2] However, the poor flux pinning property at temperatures above 30 K limits their use in high magnetic fields to low temperature operations.[3] Figure 1 summarizes the temperature and field dependence of the J_c in these materials and the requirements of some applications.[4] We can see that R123 is the most desirable material for high temperature (77K) and high field applications.

There are three major obstacles to the application of high T_c superconductors:

1) Grain boundary weak link;

2) Flux creep;

3) Manufacturing difficulties associated with the brittle ceramics.

The grain boundary weak link can be solved by formation of texture. In the Y123 system, melt-texture-growth (MTG) method has been demonstrated very successful in achieving J_c of the order of $10^4 A/cm^2$ at 77 K.[5,6,7,8] Yoo et al.[9] have achieved even

higher J_c in a magnetic field of ~1 T in melt-textured Nd123 material by processing in a low oxygen partial pressure. The practical application of this method, however, is severely hindered by its extremely slow growth rate of several millimeters per hour.[10,11] Presumably, the growth rate can be increased by the use of fine particle starting materials to decrease the diffusion distance. To solve the second problem, dispersed defects should be introduced into a superconductor as flux pinning centers. Higher J_c value of the order of $10^5 A/cm^2$ is desired for many applications. Finally, a suitable manufacturing process should incorporate the methods for texture formation and flux pinning enhancement to produce the material into the required shape (wires and tapes, etc.) and size for applications.

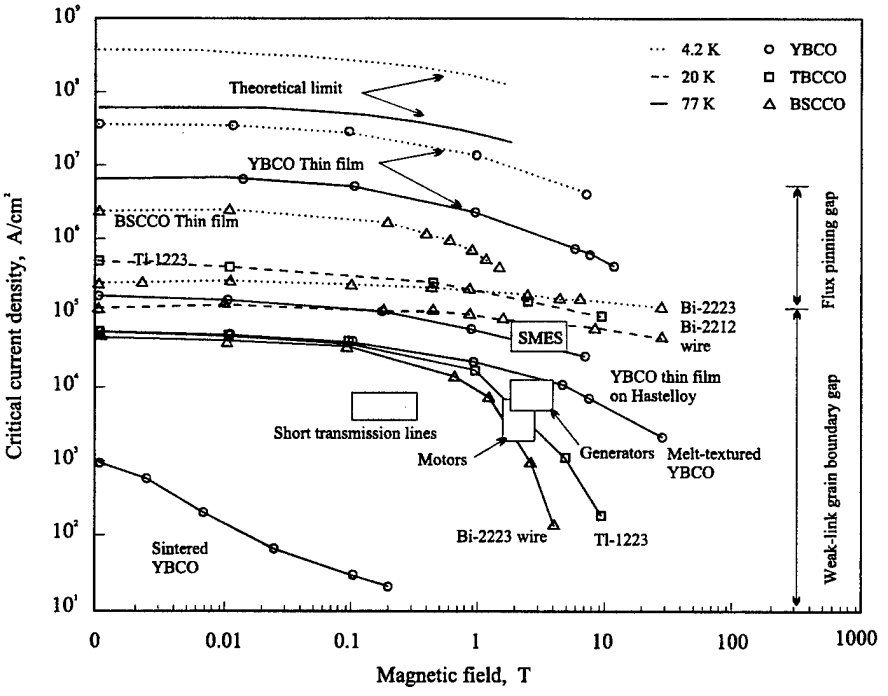

Figure 1 Critical current density of high T_c materials.[4]

This research will mainly deal with the second problem — introduction of defects as flux pinning centers in the R123 systems. Refinement of R_2BaCuO_5 (211),[7,12] addition of Pt[13,14] or $BaSnO_4$,[15] decomposition of Y124,[16] and irradiation treatments,[17] have been used to enhance flux pinning in the bulk Y123 material, but these methods have their shortcomings in that either the second phases are not fine enough or the method cannot be easily adapted to existing processing procedures.

The most practical and effective way to produce dispersed fine second phases is precipitation from a supersaturated solid solution. The size and distribution of the second phases can be tailored through suitable choice of heat-treatment. Since there is a $R_{1+x}Ba_{2-x}Cu_3O_7$ solid solution (R123ss) for the light rare earth elements (Gd, Eu, Sm, Nd and La), it is interesting to study whether a precipitation process can be used to produce flux pinning centers in these systems.

Therefore, the goal of this research is to investigate the precipitation process in R123ss as a way to introduce flux pinning centers. First, the temperature and oxygen partial pressure (Po_2) dependence of the solid solution range in R123ss will be studied. We will focus on the lower solubility limit of Nd123ss and the upper solubility limit of Gd123ss. Then, the precipitation behavior will be studied to produce dispersed second phases as flux pinning centers. Special attention will be paid to the low temperature precipitation process since extremely fine metastable precipitates may be obtained. The research results will provide guidelines for achieving high J_c in the R123 materials.

CHAPTER II LITERATURE REVIEW

1. Crystal structure and phase diagram

A. Crystal structure

The superconducting R123 phase has a deformed perovskite structure with the space group Pmmm, as shown in Figure 2.[18] Two layers of Cu-O plane are separated by a layer of rare earth ions. The anisotropy of the crystal structure determines the anisotropy of the normal and superconducting properties, and the crystal growth behavior. For example, the coherence length for Y123 is 3.2 nm in the a-b plane but only 0.4 nm along the c axis.

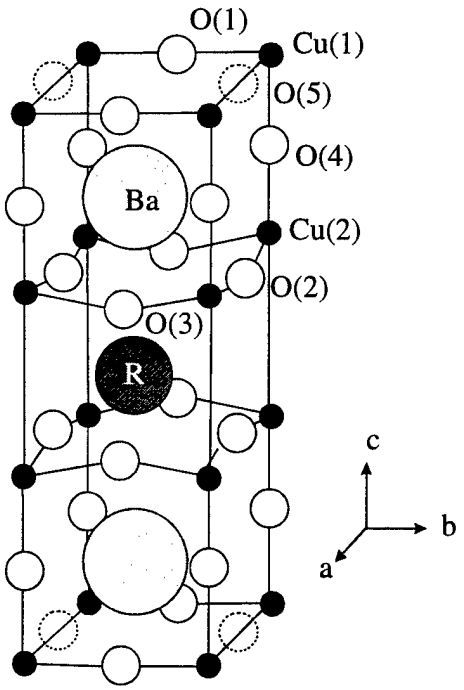

Figure 2 Crystal structure of R123.[18]

The structure and properties of Y123 is strongly related to the oxygen stoichiometry, as shown in Figure 3.[19] The oxygen content of $YBa_2Cu_3O_{7-\delta}$ compound varies from δ =0 to δ=1. The oxygen deficiency in Y123 is accommodated by oxygen vacancies formed principally on the chain sites.[20,21] The oxygen stoichiometry has a strong influence on the transition temperature (T_c). A number of authors[20,22,23] have found two plateaus of ~90 K for δ = 0 - 0.1 and ~60 K for δ = 0.25 - 0.5. Later work[21] shows a nearly linear decrease of T_c with increasing δ and this is explained in terms of oxygen ordering.

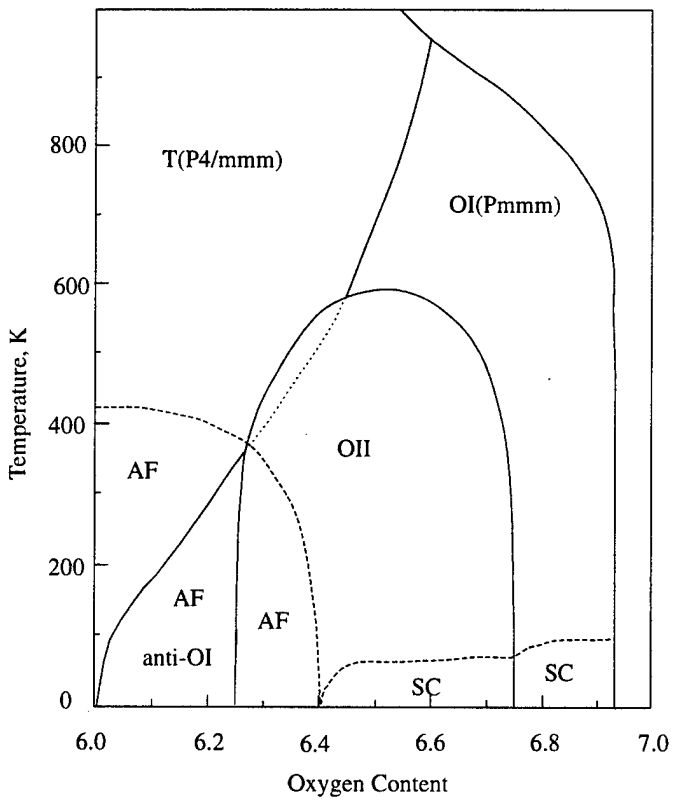

Figure 3 Structure of Y123 vs. oxygen content.[19] T: tetragonal, O: orthorhombic, SC: superconducting, AF: antiferromagnetic.

The Y site can be replaced by all rare earth elements except Pr, Pm, Ce and Tb and superconductivity is maintained.[24] The continuous decrease of the cation sizes of rare earth elements, which is known as the lanthanide contraction (Table 1), causes an almost linear decrease of the lattice parameters and the separation distance between the CuO_2 planes from the results of neutron diffraction of $RBa_2Cu_3O_7$ superconductors at 10 K.[25] For the light rare earth elements, because of their large ion size, an extended solid solution is usually formed between R and Ba (Figure 4).[26] Although the solubility ranges may be somewhat different due to different experiment conditions, the general trends are evident. The upper solubility limit is determined by the match of the ionic radii of R^{3+} to that of Ba^{2+}.[26,30] Therefore, the upper solubility will decrease with the decrease of the ionic radii of the rare earth elements. The lower solubility limits for La and Nd seem to be caused by the fact that their sizes are too bigger to fit in the Y site in the structure without simultaneous substitution into the Ba site.[26] Moreover, with the substitution of a R^{3+} for a Ba^{2+} extra oxygen must be introduced to maintain the charge balance. As a result, this will help increase the O1 site occupancy for small value of x, but as x increases further the originally empty O5 sites will by occupied and this gradually change the structure from orthorhombic into tetragonal.[27,30] Accordingly, we see an increase in T_c with x at first and then a drop of T_c for large values of x. The formation of solid solution causes decrease of T_c and very broad superconducting transition for large values of x. As extra oxygen is introduced into the solid solution when Ba^{2+} is replaced by R^{3+},[27] we may expect an oxygen partial pressure dependence of the solubility limits. Especially for Gd123ss, low oxygen partial pressure may bring the upper solubility limit to the 90 K

Table 1 Ionic radii (I.R.) of rare earth cations.[28]

R	La	Nd	Sm	Eu	Gd	Dy	Y	Ho	Er	Tm	Yb	Lu
I.R.*(nm)	0.1160	0.1109	0.1079	0.1066	0.1053	0.1027	0.1019	0.1015	0.1004	0.0994	0.0985	0.0977

* Coordination number (CN) = 8. For comparison, I.R. of Ba^{2+} is 0.142 nm(CN = 8) or 0.152 nm(CN = 10)

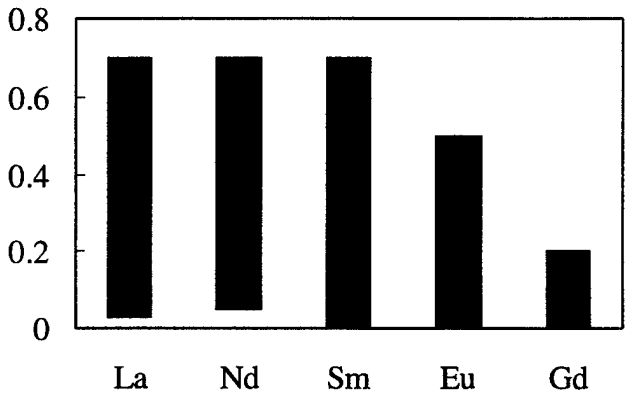

Figure 4 Solid solution ranges for the R123 systems in air.[24, 26, 29, 30]

high T_c region and this may provide us a way to obtain second phase precipitates. The high T_c phase with less Nd substitution on Ba sites is only obtainable in reduced oxygen atmosphere.[31]

There are few reports of substitution in Ba site other than by light rare earth elements mentioned above. Sr can replace up to 50% Ba with a linear decrease in T_c with concentration and K can substitute Ba up to 10% with little effect on T_c.[32]

A wide variety of elements, including Ag, Al, Co, Cr, Fe, Li, Mn, Ni, Pt, Ti, V, and Zn, can substitute into Cu sites to certain extent with the depression of T_c.[32] Ag, V appear to have the least deleterious effect on superconductivity.

B. Phase diagram and phase stability

The phase relations in R-Ba-Cu-O systems have been reviewed in detail by P. Karen, et al.[19] A summary of phase formation in R-Ba-Cu-O systems is given in Table 2. Some typical subsolidus phase diagrams for R-Ba-Cu-O in oxygen are shown in Figure 5. Besides the formation of R123ss for La, Nd, Sm, Eu and Gd, the phase relationships also change in these systems. The R_2CuO_4 (201) phase can only be prepared with the large size of R from La to Gd, while $R_2Cu_2O_5$ (202) compound forms for the smaller size of R. For Nd and Sm, the tie-line connection runs through R123ss and 201, but for Eu and smaller cations the tie-line connects 211 and CuO.

Table 2 Summary of Phase formation in $RO_{1.5}$-BaO-CuO systems in oxygen or air.[30,33]

R	La	Pr	Nd	Sm	Eu	Gd	Dy	Y	Ho	Er	Tm	Yb	Lu
R_2O_3-CuO													
R_2CuO_4	O	O	O	O	O	O	X	X	X	X	X	X	X
$R_2Cu_2O_5$	X	X	X	X	X	X	O	O	O	O	O	O	O
R_2O_3-BaO													
R_2BaO_4	O	O	O	O	O	O	O	O	O	O	X	X	X
$R_4Ba_3O_9$	X	X	X	O	O	O	O	O	O				
$R_2Ba_2O_5$	X	X	X										O
$R_2Ba_4O_7$	X	X	X										O
$RBaO_3$		O											
R_2O_3-BaO-CuO													
123	O	O	O	O	O	O	O	O	O	O	O	O	O
211	X	X	X	O	O	O	O	O	O	O	O	O	O
422	O	X	O	X	X	X	X	X	X	X	X	X	X
143	X	X	X	O	O	O	O	O	O	O	O	O	O
163	X	X	X	O	O	O	O	O	O	O	O	O	O
415	O	X	X	X	X	X	X	X	X	X	X	X	X

O: Phase formation; X: No phase formation

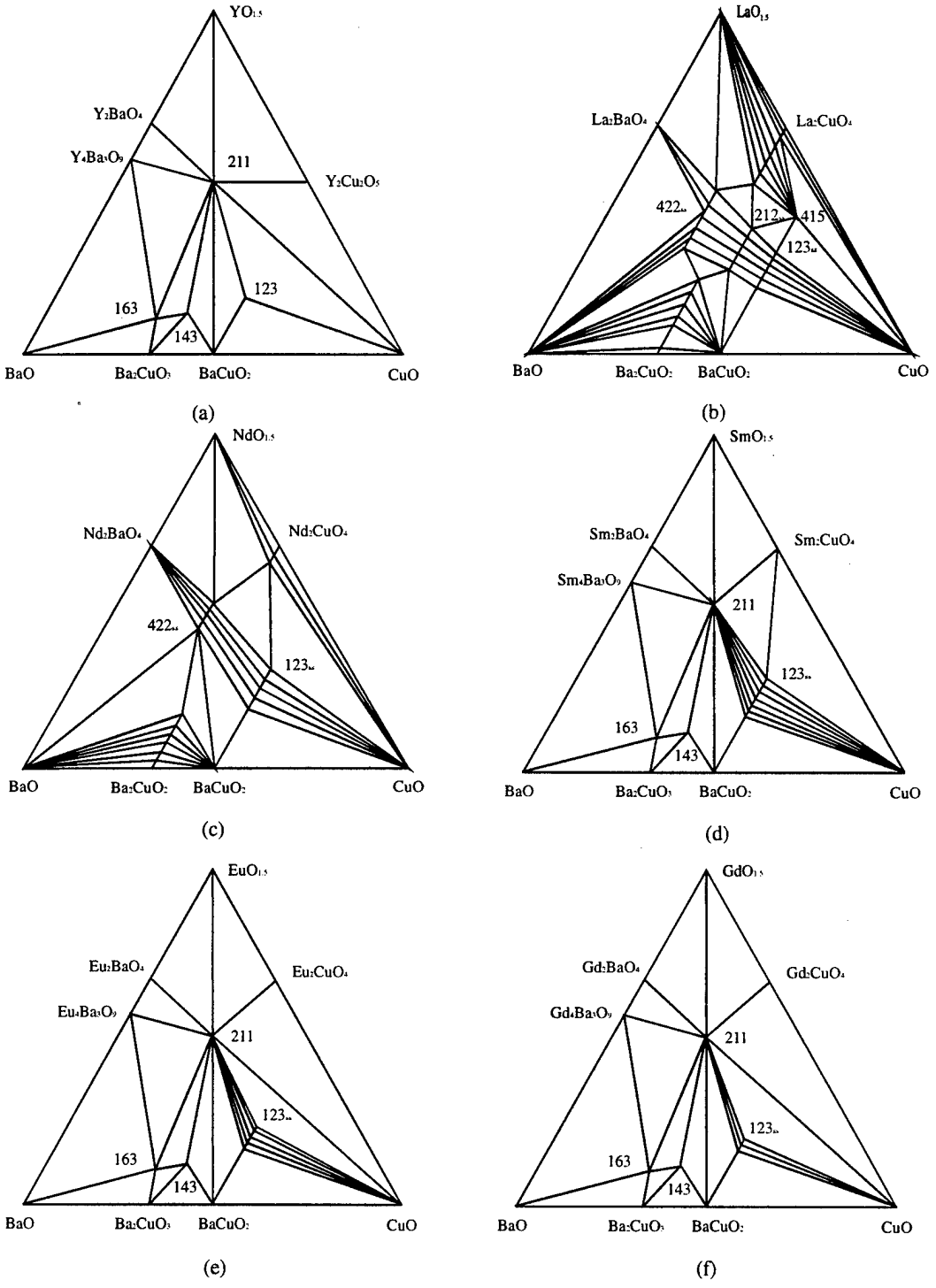

Figure 5 Subsolidus phase diagrams of R-Ba-Cu-O in oxygen. (a) Y-Ba-Cu-O at 900°C,[19] (b) La-Ba-Cu-O at 950°C, [19,31] (c) Nd-Ba-Cu-O at 950°C, [19,33] (d) Sm-Ba-Cu-O at 950°C, [19,30,33] (e) Eu-Ba-Cu-O at 950°C,[19] and (f) Gd-Ba-Cu-O at 950°C.[30,34]

The solidus-liquidus equilibrium diagram is very useful for the successful growth of single crystal and for the MTG method. The complexity in this system usually limits the investigation only in certain vertical sections. Aselage and Keefer[35] have studied the invariant reactions in the most useful Cu-rich corner (Table 3) and a liquidus projection is shown in Figure 6. The most useful vertical section across 211 and 123 is given in Figure 7. It can be seen that in air Y123 melts incongruently at 1015°C to 211, which in turn melts to Y_2O_3 at 1270°C. Research on the other RE system suggests similar behavior.[36] But the melting point is much higher for the light rare earth R123 (Table 4). The melting point also decreases with decreasing oxygen partial pressure.[36]

Table 3 Invariant reactions in Y-Ba-Cu-O in air.[35]

Temperature, °C	Invariant point	Reaction
890	e1	$YBa_2Cu_3O_{6+w} + BaCuO_2 + CuO = L$
920	e2	$BaCuO_2 + CuO = L$
940	p1	$YBa_2Cu_3O_{6+w} + CuO = Y_2BaCuO_5 + BaCuO_2 + L$
975	p2	$Y_2BaCuO_5 + CuO = Y_2Cu_2O_5 + L$
1000	e3	$Y_2BaCuO_5 + BaCuO_2 = L$
1000	p3	$YBa_2Cu_3O_{6+w} + BaCuO_2 = Y_2BaCuO_5 + L$
1015	m1	$YBa_2Cu_3O_{6+w} = Y_2BaCuO_5 + L$
1015	m2	$BaCuO_2 = L$
1026		$CuO = Cu_2O$
1110	e4	$Y_2Cu_2O_5 + Cu_2O = L$
1122	m3	$Y_2Cu_2O_5 = Y_2O_3 + L$
1270	m4	$Y_2BaCuO_5 = Y_2O_3 + L$

Table 4 Melting temperature (T_m) of R123 in air.[37]

R	La	Nd	Sm	Eu	Gd	Dy	Y	Ho	Er	Tm	Yb	Lu
T_m (°C)	1090	1090	1060	1050	1030	1010	1000	990	980	960	900	880

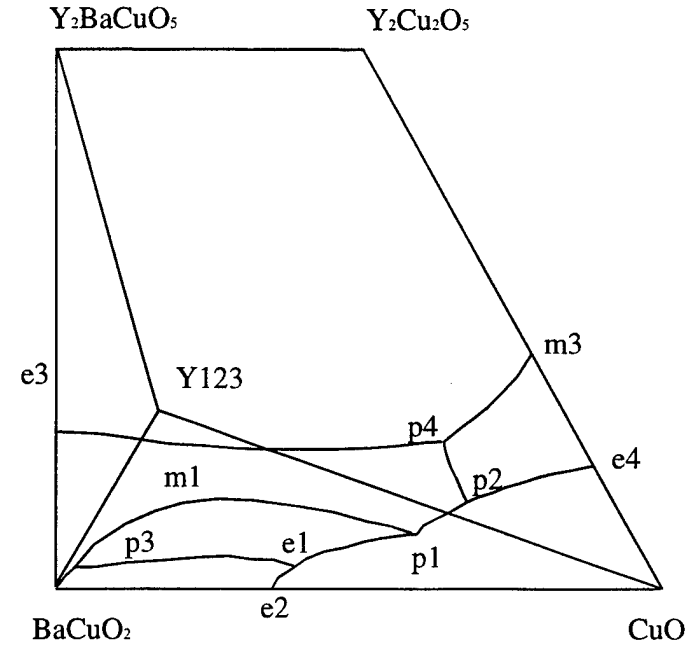

Figure 6 Liquidus projection in Y-Ba-Cu-O in air.[35]

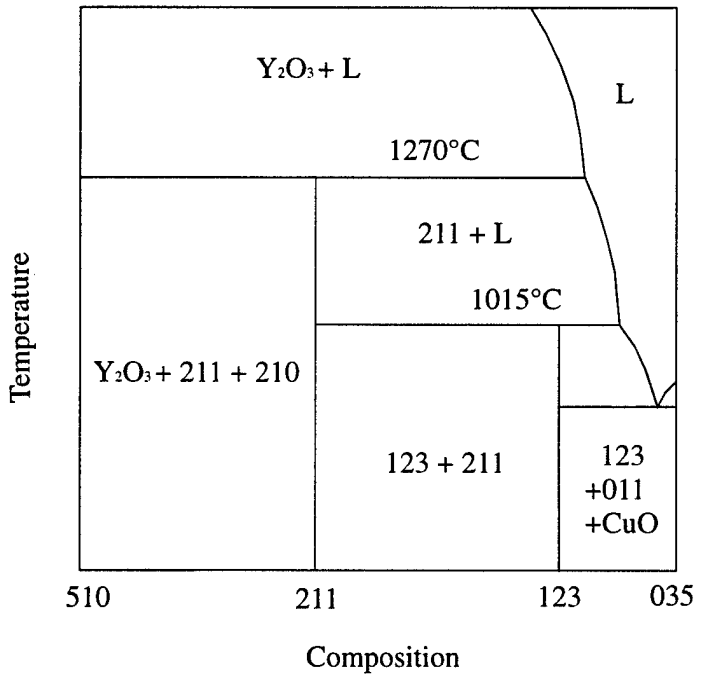

Figure 7 A vertical section of Y-Ba-Cu-O phase diagram in air.[35]

It is interesting to notice that there is a temperature dependence of the solid solubility limits in Nd123ss (Figure 8).[33] The maximum lower solubility limit is x = -0.1 at bout 990°C in air and it is decreased to x = 0.07 at 900°C. If we prepare a solid solution with x = -0.1 at 990°C, we should expect the precipitation of $BaCuO_2$ as a second phase at 900°C. This may provide an effective way to introduce flux pinning centers in Nd123 system. The formation of solid solution with composition of x = -0.1 is different from the normal substitution of rare earth cations into Ba site. However, cautions should be taken since the solid solution range may be over-estimated from a simple X-ray diffraction phase identification method.

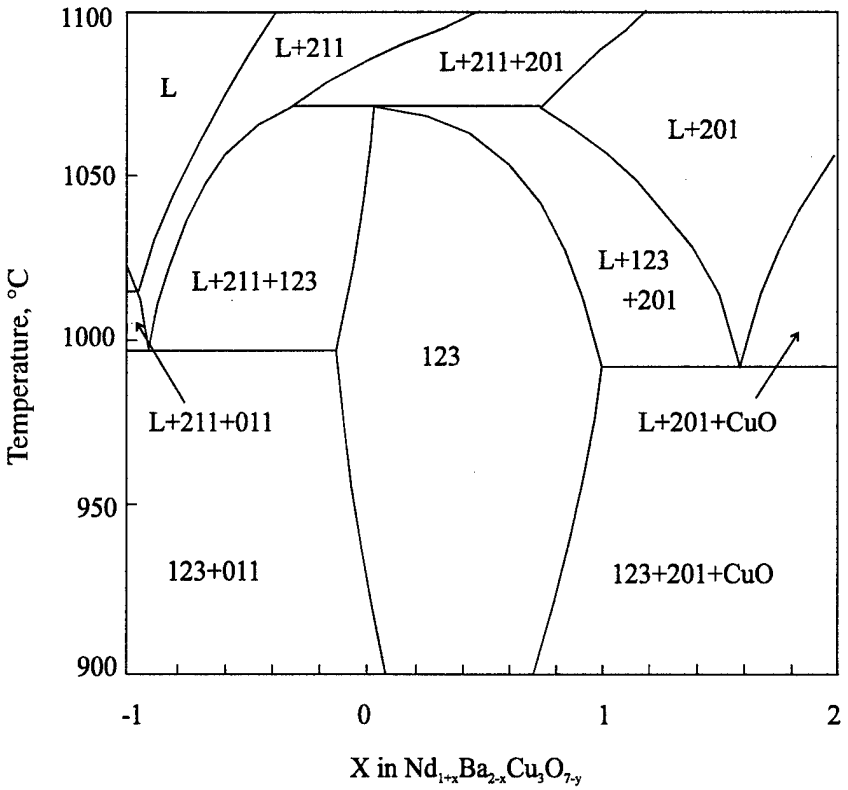

Figure 8 Temperature-concentration section of Nd-Ba-Cu-O system in air along $BaCuO_2$ and Nd123.[33]

The phase stability of Y123 has been studied by several groups.[38,39,40,41] As shown in Figure 9,[41] Y123 phase is only stable in certain temperature and oxygen partial pressure range. At high oxygen partial pressure, it decomposes to 211, 023 and CuO. At low oxygen partial pressure, it will decompose into 211, 012 and 132 phases. At high temperature it will melt incongruently to 211. The low temperature stability of Y123 remains unclear due to the slow kinetics at room temperature or below. However, phase diagram calculation predicts the existence of separate ordered phases at low temperature.[42]

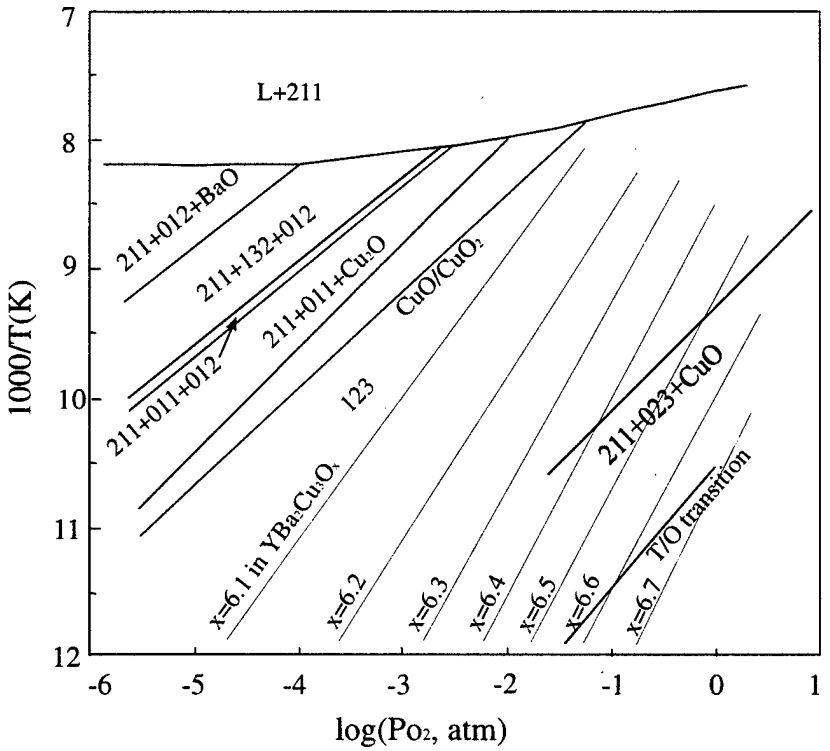

Figure 9 Phase stability of Y123.[41]

It should be pointed out that oxygen partial pressure plays an important role in the phase relations. Actually oxygen (gas) always co-exists with other condensed phases although it is not always listed in the phase diagrams and the phase reactions. All the phase diagrams shown above are some projections of oxygen iso-activity cuts of the R-Ba-Cu-O phase diagrams. As the free energies of all the phases are affected by the oxygen partial pressure, the phase diagram changes with oxygen partial pressure accordingly. It is generally found that the melting temperatures of 123 and 211 phases are lowered in low oxygen partial pressure. It is even found the relative relationship of phases in Sm-Ba-Cu-O changes with the oxygen partial pressure along with a decrease of upper solubility limit (Figure 10).[43] The upper solubility limit of Gd123ss is decreased to x = 0.04 at 900°C and 950°C in 1% oxygen atmosphere with the highest T_c of ~ 95 K in the system.[43,44] Beyond the solubility limit, dispersed second phases will precipitate from the solid solution which may act as flux pinning centers.

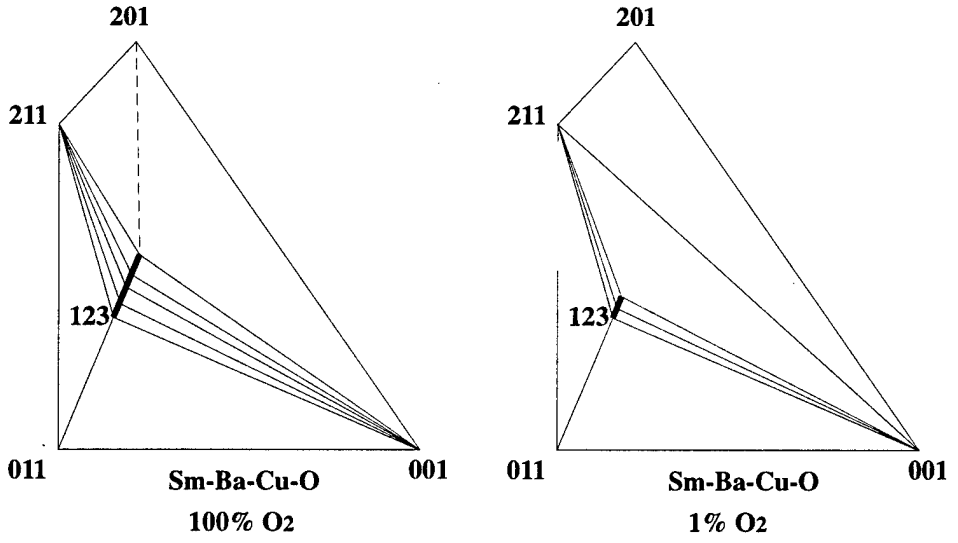

Figure 10 Phase relation of Sm-Ba-Cu-O in 100% oxygen and 1% oxygen at 950°C.[44]

2. Diffusion in R123

Diffusion is a fundamental process for the kinetics of phase transformation. In one dimension, diffusion obeys the diffusion equation:

$$\frac{\partial}{\partial x}(D\frac{\partial C}{\partial x}) = \frac{\partial C}{\partial t}$$

Where C is the concentration of the diffusing species, x the diffusion distance, t the diffusion time, and D the diffusion coefficient. There are two kinds of diffusion coefficients, chemical diffusion coefficient ($\tilde{D}$) and tracer diffusion coefficient (D^*). Chemical diffusion coefficient is related to diffusion under a chemical gradient and is usually studied by relaxation experiment ($\tilde{D} = x^2/6t$). D^* describes diffusion without a chemical gradient and is more directly correlated with atomic transport mechanisms. The two are related by

$$\tilde{D} = D^*(1+\partial \ln \gamma / \partial \ln C)$$

Where γ is the activity coefficient of the diffusant and the term in brackets is the thermodynamic factor. When there is no confusion, D is used for both for simplicity.

Since the oxygen stoichiometry is related to the superconducting properties, the diffusion of oxygen has been studied by a number of researchers, as reviewed by Routbort and Rothman.[45] The main conclusions are

1) Diffusion is anisotropic with $D_c << D_{ab}$,

2) At high oxygen content, $D_b >> D_a$,

3) For polycrystals, $D \approx D_{ab}$.

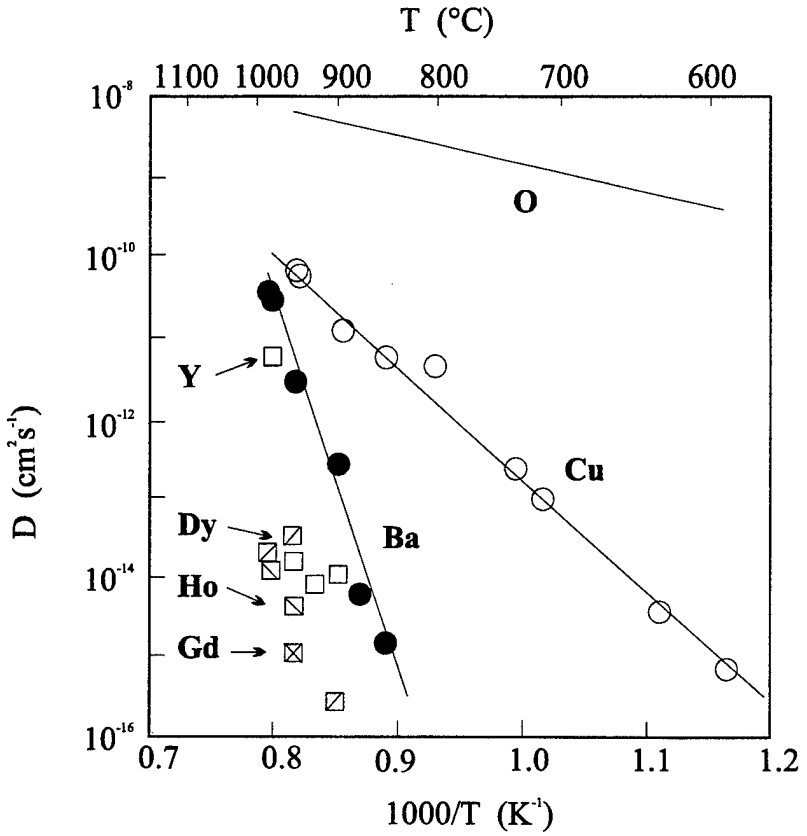

Figure 11 Tracer diffusion coefficients in Y123 and other R123.[45,47]

The tracer diffusion coefficient of oxygen in polycrystals is shown in Figure 11 and the corresponding thermodynamic factor can be approximated as $1/\delta$ in $YBa_2Cu_3O_{7-\delta}$.[46] The thermodynamic factor gives rise to a drastic enhancement of the chemical diffusion coefficient near $\delta = 0$.

The diffusion of other species in Y123 has also been studied by tracer diffusion experiment (Figure 11).[47] It can be seen that $D_{Cu} > D_{Ba} > D_Y$. Again it is found that there is a large anisotropy in diffusion. Diffusion of Ba along the c axis is at least three orders of magnitude slower than diffuison in the ab-plane. The tracer diffusion coefficient of O

is not affected by Po_2.[45] The enhanced diffusion for Cu, Ba and Y observed in sintering and creep in lower Po_2 is attributed to generation of an alternative diffusion path.[47]

3. Grain boundary weak link

A. The nature of weak link

Soon after the discovery of high temperature superconductor, it is found that the transport J_c of polycrystalline material is very low and has a strongly field dependent deterioration. This suggests that most high angle grain boundaries are weak linked.[48,49,50] In such a superconductor, the low field behavior is dominated by intergrain shielding currents, but at high field the grains become decoupled from each other and the magnetization is essentially due to the intragranular currents.[51]

The exact nature of the grain boundary weak link is not well known, but is related to the short coherence length. Earlier reports suggest that microcrack from anisotropic expansion and the tetragonal-orthorhombic transition, second phases, amorphous layers are responsible for the low J_c. These may be part of the reason for low J_c, but the weak link behavior of clean grain boundaries can not be explained.[52] Cation compositional deviations at the grain boundaries are supposed to be the cause of weak link.[53] The hydrostatic strain around boundary dislocation[54] or the charge imbalance introduced by dislocation core[55,56] is also suggested to suppress the order parameter on grain boundary.

Dimos et al.[49] studied the grain boundaries of thin film bicrytals and they found that all the grain boundaries with misorientation angle greater than about 5-10° are weak linked. The work on the grain boundaries in flux-grown bicrystals by Babcock et al.[57,58]

and Eom et al.[59] also shows general tendency for grain boundaries to change from flux pinning to Josephson junction to purely resistive behavior as the misorientation angle increases. However, they also found that the grain boundary properties cannot be predicted on the basis of the misorientation angle alone. Some special high angle boundaries are strongly coupled, which can be explained in terms of the near-coincident-site lattice (NCSL) orientation.[60] The existence of the liquid phase in the flux growth method may help the formation of such strongly coupled high angle grain boundaries.

A grain boundary of NCSL orientation is a boundary of low interface energy. Since such a boundary has low energy, thermodynamically there is a natural tendency to change a higher energy boundary into a low energy boundary provided that the atoms involved have enough mobility. When the mismatch angle is very small, it is easy to obtain the low energy configuration. When the mismatch is too big, it is difficult to get such configuration except that the mismatch happens to be near one of the few special angles. One such special angle is the angle of twin boundary, which is usually strongly coupled. From the consideration of processing, therefore, two conditions are necessary for overcoming the weak link grain boundary problem in bulk materials: (1) formation of texture and (2) the existence of liquid phase during processing.

B. Melt-texture growth

Melt-texture growth method has been very successful in overcoming the weak link problem.[5,6,7,8] The basic process involves the melting of 123 phase above its peritectic temperature, followed by slow cooling through the peritectic temperature when oriented 123 grains form with 211 inclusions distributed throughout the superconducting

matrix (refer to Figure 7). However, the formation of 123 does not follow the usual peritectic reaction process, instead it nucleates in the liquid and grows by diffusion of Y through the liquid from the dissolution of 211.[10,11] The 123 grain will grow preferentially in the a-b plane. Because of the sympathetic nucleation of new 123 grains on the old ones, textured domains are formed. If a temperature gradient is used, uniform grain alignment over long length can be achieved.

The practical application is severely hindered by the extremely slow growth rate of several millimeters per hour due to the long range diffusion of Y.[10,11] Reducing the size of 211 can increase the growth rate. But the success in increasing growth rate is very limited for various modifications such as quenching in the melt-powder-melt growth,[7] doping of Pt [13,14] and $BaSnO_3$.[15]

C. Other texture processing

a. Epitaxy-induced texture

Since the J_c of thin film is very high, the epitaxial thin film deposition technique may be used for bulk material. Usually a buffer layer is deposited on a metallic substrate, and the Y123 film is deposited on the buffer layer. Y123 film deposited by laser ablation has shown J_c of 2.5×10^5 A/cm^2 at 77K and 0 T.[61] Two problems that need to be addressed are the slow deposition speed and the small superconducting volume fraction.

This method has been adapted to the production of flexible superconducting tapes.[62,63,64] In the ion beam assisted deposition (IBAD) process developed at Los Alamos National Laboratory, two beams of charged particles are used to grow yttria-stablized zirconia (YSZ) with (100) orientation on top of a cerium oxide-buffered Hastelloy tape.

Then a Y123 thin film is deposited on the YSZ surface. In the rolling-assisted, biaxially-textured substrate (RaBiTS) process developed at Oak Ridge National Laboratory, a biaxially-textured nickel substrate strip is produced by rolling, then cerium oxide and YSZ buffer layers are deposited and finally Y123 thin film is obtained on the YSZ buffer layer by pulsed-laser deposition. Both processes have produced tapes with J_c of 1.5-$3x10^5 A/cm^2$ at 77K and 1T. Again the challenge is how to make the process scalable for mass production of long length superconducting tapes.

b. Magnetic alignment

Y123 can be aligned in a magnetic field due to its anisotropic paramagnetic susceptibility at normal state.[65] The anisotropy characteristics of paramagnetic susceptibility of some R123 are list in Table 5.[66,67,68] The superconducting powder is suspended in an organic liquid (e.g. heptane) while aligned with a magnetic field of about 4T. After the liquid evaporates, the material can be removed from the field and sintered at high temperature. But the final sintered material is mostly weak linked. Some liquid aided sintering is necessary to increase the coupling between grains.

Table 5 Anisotropy of paramagnetic susceptibility of some R123.[66,67,68]

R in R123	Anisotropy	Orientation
Y, Dy, Ho, Nd	$\chi_{//c}>\chi_{\perp c}$	c // H
Er, Eu, Gd	$\chi_{//c}<\chi_{\perp c}$	c $\perp$ H

c. Deformation texture

The powder-in-tube process is very successful for the Bi-Sr-Ca-Cu-O wires and tapes.[1,2] The success in the Bi system relies on the partial melting treatment between deformations. During the repeated deformation and sintering process, deformation, interface reaction and liquid phase all contribute to the formation of the textured and coupled grains.[1,2] However, this process cannot be applied to R123 since their melting points are above or very close to that of silver. As expected, most of these boundaries in deformation textured Y123 are found to be weakly coupled.[49] Without a liquid phase, it is difficult to form strong coupling between grains.

d. Geometry-induced texture

Since the growth of 123 occurs preferentially in the a-b plane along the <110> direction, if the material is melt-textured in a confined geometry, the 123 phase will grow along the length direction.[69] But the reaction of the liquid with substrate at that high peritectic temperature will exclude most substrate materials.

4. Flux pinning

Although the J_c of melt-textured Y123 has reached high values, further enhancement to the level > 10^5 A/cm^2 and improved behavior in high magnetic field are strongly required for practical applications. On the other hand, the J_c values of bulk materials are still two orders of magnitude lower than that of thin films and irradiated Y123 single crystals. Therefore, it is necessary and possible to increase J_c by introducing more effective flux pinning centers.

A. Pinning force

If a magnetic field larger than the lower critical magnetic field is applied to a type II superconductor like high T_c superconductors, magnetic flux will penetrate the superconductor as flux quanta Φ_0 (Φ_0 = 2.0678×10^{-7} G·cm^2 = 2.0678×10^{-15} weber), having a normal core of radius of coherence length ξ and being circulated by a supercurrent in a radius of penetration depth λ. The flux quanta will form a vortex lattice. The spacing between two adjacent flux quanta in a regular lattice is listed in Table 6 (this provides an estimate of the required defect density for flux pinning). The vortices are pushed by the Lorentz force from the supercurrent. If the vortices are moved as a result of this force, an electric field is generated along the direction of the supercurrent and then power dissipation appears. Therefore, it is necessary to pin the vortices from motion.

Table 6 The spacing of flux quanta vs. magnetic field

Magnetic field (T)	0.1	0.5	1	2	5	10	15
Flux quanta spacing (nm)	218	97	69	49	31	22	18

The problem of flux pinning consists of three issues:

1) The elementary interactions between a flux line and various defects;

2) The elastic and plastic properties of the vortex lattice;

3) Summation of the individual contributions of flux pinning centers.

As a vortex enters the superconducting region, the free energy density at the vortex core is increase by $\frac{B_c^2}{2\mu_o}$. Therefore, a vortex in a normal region with volume V will experience a pinning potential

$$U_p = \frac{B_c^2}{2\mu_o} \cdot V$$

where B_c is the thermodynamic critical field and ξ is the Ginzburg-Landau coherence length.

or $U_p = \frac{B_c^2}{2\mu_o} \cdot \frac{4\pi}{3} \xi^3$ for small pinning sites comparable with ξ

$U_p = \frac{B_c^2}{2\mu_o} \cdot \pi \xi^2 d$ for big pinning sites with length d along the field

Murakami[12] used this to argue that big defects may be more effective since the pinning potential for small pinning sites is around 0.01eV, almost comparable to the thermal energy at 77K. Since only the length along the fuxoid is included in the equation, needle-shaped defects are desired as in the case of columnar defects produced by irradiation.

The elementary pinning force is given as

$$f_p = \frac{dU_p}{dx}$$

$f_p = \frac{B_c^2}{2\mu_o} \cdot \frac{4}{3} \pi \xi^2$ for small pinning sites

$f_p = \frac{B_c^2}{2\mu_o} \cdot \pi \xi d$ for big pinning sites

Here we assume that the interface is very sharp. But If the pinning potential changes gradually over the interface, the pinning force will become smaller. As the coherence lengths are very small for oxide superconductors, precipitates will be in the category of big pinning sites and we will use only the equations for big sites afterwards.

If we take into account the anisotropy of the oxide superconductors, the elementary pinning force should be modified as

$$f_p = \frac{B_c^2}{2\mu_o} \cdot \pi \xi_{ab} d \qquad \text{for H // c or H } \perp \text{ c but Lorentz force // c}$$

$$f_p = \frac{B_c^2}{2\mu_o} \cdot \pi \xi_c d \qquad \text{for H } \perp \text{ c but Lorentz force } \perp \text{ c}$$

In a large magnetic field, the reduction of the order parameter must be taken into account and f_p is modified as[12]

$$f_p = \frac{B_c^2}{2\mu_o} \cdot \pi \xi d (1 - \frac{B}{B_{c2}})$$

The bulk pinning force is

$$F_p = \sum f_p \text{ and } F_p = J_c \cdot B$$

If the vortex lattice is very rigid, the bulk pinning force will be almost zero. It is believed that the flux line lattice of the oxide superconductor is very soft and direct summation may be assumed.[12] For a sample with defect number density of N_p and volume fraction of V_f, we get an expression for J_c at high field:[12]

$$J_c = \frac{\pi B_c^2 \xi}{4\mu_o} \cdot \Phi_o^{-\frac{1}{2}} \cdot B^{-\frac{1}{2}} \cdot N_p d^2 (1 - \frac{B}{B_{c2}})$$

$$J_c \sim N_p d^2$$

For uniaxial defects, $V_f=N_p d^3$, we have

$$J_c \sim \frac{V_f}{d}$$

For needle-shaped defects with diameter of about 2ξ, $V_f=N_p \xi^2 d$, we have

$$J_c \sim \frac{V_f \cdot d}{\xi^2}$$

Therefore, we prefer long needle-shaped defects with sharp interface along the field direction for strong flux pinning.

The critical current density is usually obtained by Bean's model[70] from the hysteresis loop

$$J_c = \frac{30 \cdot (M_- - M_+)}{D}$$

where J_c (A/cm^2) is the critical current density, M_+ and M_- are the magnetization (emu/cm^3) during increasing and decreasing field respectively and D (cm) is sample diameter or grain size depending on the connectivity of the sample.

In consideration of the anisotropy of the high T_c superconductors, the equation is modified as following for a sample with dimension $a \times b \times c$ (cm^3) (a<b, c is the dimension along the c-axis):[71,72]

$$J_c = \frac{20 \cdot (M_- - M_+)}{a \cdot (1 - \frac{a}{3b})} \qquad \text{for H // c-axis}$$

$$J_c \approx \frac{20 \cdot (M_- - M_+)}{a} \qquad \text{for H } \perp \text{ c-axis and thick samples.}$$

B. Intrinsic pinning

For a applied field directed along the a-b planes, the enhancement in J_c is attributed to the anticipated intrinsic pinning of the insulating region between the Cu-O layers.[73,74] In this situation, the magnetic vortexes with elliptical cores of dimensions roughly about coherence length lie in the insulating layers. With the field parallel to a-b plane, the Lorentz force moves in the c direction. Thus the insulating layers resist the movement of magnetic vortices across these layers, providing effective intrinsic pinning.

C. Extrinsic pinning

In order to increase J_c of type II superconductors, defects must be introduced as flux pinning centers. In R123, these defects include oxygen defects, dislocations, twin planes and stacking faults, and non-superconducting phases.

The "fishtail" peak in magnetization hysteresis of oxygen deficient Y123 single crystal is suggested to be caused by the flux pinning due to oxygen defects.[75] However, it is also found that the peak in melt-textured Y123 is not originated from oxygen defect.[76] Since well annealed samples still have large J_c, it seems that oxygen defects are not important pinning centers.[12]

In thin film, Mannhart et al.[77] find J_c enhancement with dislocation density on c-axis oriented 123 films with current flowing along the a-b planes with H //C (intrinsic pinning is irrelevant in this case). For melt-textured Y123 materials, the measurement of dislocation density gives contradictory results.[12,78] Since dislocation may be created during sample preparation, definite conclusion can not be drawn. From the thin film result, high density of dislocations may be effective pinning centers at high field.

Twins and stacking fault are planar defects. They are only effective when flux is parallel to the plane and the Lorentz force acts perpendicular to the plane. Even in such favorable condition, the effect of twins is shown to be small.[12]

Fine dispersed 211 phase can act as effective pinning sites in MTG Y123.[12] But for a strong flux pinning, further decrease of the size of 211 phase is required. Recently, strong flux pinning is observed in Nd123 melt-textured in low oxygen partial pressure.[9] Detailed study is needed to determine the effective flux pinning centers. S. Jin et al[16] have achieved significantly improved flux pinning by decomposing Y124 (stable at <800°C) to Y123. Therefore, precipitation is a very useful method for the enhancement of flux pinning.

The most useful information about flux pinning centers comes from the study of the effect of artificially created defects in single crystal, as reviewed by Kirk and Weber.[17] Columnar defects caused by heavy ion irradiation are found to be the most effective in flux pinning. It is also suggested that splayed columnar defects have even better effect.[79]

5. Precipitation[80,81,82,83]

Precipitation from a supersaturated solid solution is by far the most widely used method for producing a dispersed second phase. The precipitation process may be divided into three stages: 1) nucleation, 2) growth of nuclei, and 3) coarsening of the precipitate without change in its volume fraction.

The free energy change associated with the nucleation process of volume V of the second phase consists of a reduction of volume free energy $V\Delta G_v$, increase of surface energy $A\gamma$, and a misfit strain energy $V\Delta G_s$.

$\Delta G = -V(\Delta G_v - \Delta G_s) + A\gamma$

For an isotropic spherical second phase of radius r

$\Delta G = -(4/3)\pi r^3(\Delta G_v - \Delta G_s) + 4\pi r^2\gamma$

Therefore we can get the critical radius r^* for nucleation and the nucleation barrier ΔG^*

$r^* = 2\gamma/(\Delta G_v - \Delta G_s)$

$\Delta G^* = 16\pi\gamma^3/[3(\Delta G_v - \Delta G_s)^2]$

As ΔG_v is strongly temperature dependent, ΔG^* will also be strongly temperature dependent and it decreases as the temperature decreases.

The homogeneous nucleation rate can be described as[81]

$N_{hom} = \omega C_0 \exp(-\Delta G_m/kT)\exp(-\Delta G^*/kT)$

ω: frequency factor

C_0: number of atoms per unit volume.

ΔG_m: activation energy for atomic migration.

For heterogeneous nucleation, some free energy ΔG_d will be released from the defect to reduce or even remove the activation energy barrier ΔG^*.[81]

$N_{het}/N_{hom} = (C_1/C_0)\exp[(\Delta G^*_{hom} - \Delta G^*_{het})/kT]$

where C_1 is the heterogeneous nucleation sites per unit volume.

Generally speaking, grain boundary is effective in reducing the volume and surface area of critical nuclei. The main effect of dislocation is to reduce the strain energy. ΔG_d is relatively small for vacancies but vacancies can increase diffusion rates and relieve misfit strain energy. Coherent or semicoherent interfaces are formed

whenever possible to reduce the interface energy γ. At low temperature, GP zone and other transition phases may form due to their lower interface energy. It is instructive to consider the precipitation sequence of Al-Cu alloy, as shown in Figure 12.[81] The fastest transformation rates are associated with the higher nucleation rates and therefore the finest precipitate distributions. GP zone may be formed by the spinodal decomposition where there is no thermodynamic barrier to decomposition.

The interplay between volume free energy, interface energy and strain energy will determine the phase, position and shape of the precipitate. The nucleation sequence observed in most alloys are listed in Table 7.[80]

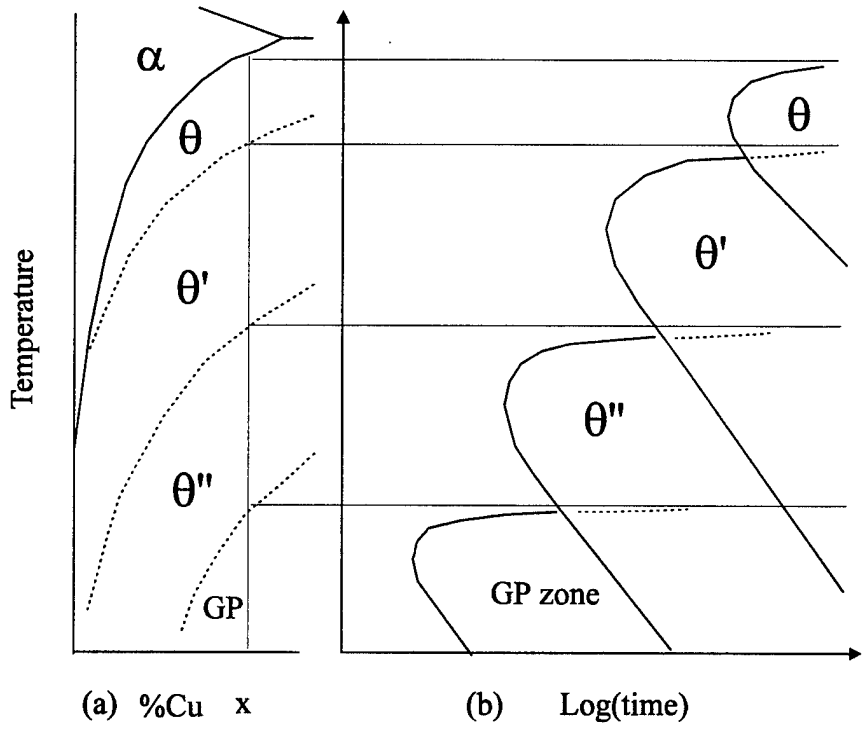

Figure 12 (a) Schematic metastable solvus of Al-Cu alloy and (b) precipitation starting time at different temperatures for alloy composition x.[81]

Table 7 Nucleation sequence observed in alloys.[80]

noncoherent nuclei	grain boundary > dislocation > matrix
semicoherent nuclei	dislocation > matrix > grain boundary
	dislocation > grain boundary > matrix
coherent nuclei with a strain field	dislocation > matrix > grain boundary

For a noncoherent interface, the surface energy will be minimal for a spherical shape but the misfit strain energy will favor a disk or needle-like shape. For a semicoherent or coherent interface, a plate-like shape is usually formed with certain orientation relationship with the matrix. The strain energy will favor a spherical second phase if the second phase is harder otherwise a disc shape is preferred. In addition, elastic anisotropy will tend to produce disc perpendicular to the soft direction of the matrix. Since the coherence length of the oxide superconductor is very small, we should avoid grain boundary precipitation. To get strong flux pinning, dispersed and elongated precipitate is also desired. Therefore, low temperature coherent precipitation seems to offer the best possibility.

The overall transformation kinetics can be described by a modified Avrami equation[81]

$$f = 1-\exp(-kt^n)$$

where f is the fraction transformed

k is related to the nucleation and growth mechanism

n=1~4 and n is temperature dependent.

After the precipitation reaction, a high density of small precipitates will tend to coarsen into a low density of larger particles to minimize the surface energy. Larger particles tend to grow at the expense of small particles due to the Gibbs-Thomson effect. It has been shown that the rate of coarsening is related to the product of $D\gamma X_e$,[81] where D is the diffusion coefficient, γ the interfacial energy and X_e the equilibrium solubility of very large particles.

CHAPTER III EXPERIMENTAL PROCEDURES

1. Precipitation in Gd123ss

The phase stability range of Gd123 was first determined by DTA (differential thermal analysis) and XRD (X-ray diffraction) in different oxygen partial pressures. This will set the limits of the temperature and Po_2 for thermal processing. Then DTA was used to determine the liquid formation temperatures. The precipitation reaction was conducted at lower temperatures to obtain fine precipitates. J_c will be determined from the hysteresis measurement. This can be related to the size and distribution of second phases in different processing conditions. The microstructure will be observed by optical microscopy, SEM (scanning electron microscopy) and TEM (transmission electron microscopy).

The equilibrium reaction is

$$R_{1+x}Ba_{2-x}Cu_3O_7 = \alpha\, R_{1+y}Ba_{2-y}Cu_3O_7 + \beta\, R_2BaCuO_5 + \gamma\, CuO$$

where $\alpha=(1-x)/(1-y)$

$\beta=(x-y)/(1-y)$

$\gamma=2(x-y)/(1-y)$

The volume fraction of second phases can be calculated by

$$V_s=(\beta\bullet M_{211}/\rho_{211}+\gamma\bullet M_{CuO}/\rho_{CuO})/(\alpha\bullet M_{123ss}/\rho_{123ss}+\beta\bullet M_{211}/\rho_{211}+\gamma\bullet M_{CuO}/\rho_{CuO})$$

where M and ρ are the molar mass and density of the corresponding phase.

For Gd123ss with x = 0.2 and y = 0.05, we get V_s = 18%.

Gd123ss with x = 0.2 was prepared by a solid state reaction method from Gd_2O_3,

$BaCO_3$ and CuO. After being calcined three times in CO_2-free air at 890-900°C for 24 hr with intermediate grinding, the material was pressed into pellets of about 1g each and was sintered at 980°C in oxygen for 24 hr. This temperature was chosen to avoid a liquid formation at 990°C determined by DTA for the precursor powder. The pellets are ~87% dense and the grain size is around 5μm. Gd123 was prepared in a similar way except that a higher sintering temperature of 1025°C was used since the melting temperature of Gd123 is about 1067°C in oxygen. The sintered Gd123ss samples were used for treatment in low oxygen partial pressures at the ambient total pressure. Nitrogen and oxygen were mixed in a calibrated flow controller to get the required Po_2. The oxygen partial pressure was monitored by a zirconium oxide oxygen analyzer. The oxygen volume fraction (in percentage and ppm) and absolute oxygen partial pressure (in the unit of bar) are both used to describe the oxygen partial pressure. A specially designed sample holder was used for quick change of Po_2 environment of the sample.

Gd123ss ($x = 0.2$) samples were treated at 870°C, 850°C and 800°C in 300 ppm oxygen for 24hr and at 800°C, 750°C and 700°C in nitrogen ($Po_2 = 30$ ppm) for 24hr, and followed by quenching in the same atmospheres. Then all the samples were subject to an oxygen annealing. The samples were held at 600°C for 2 hr, continuously cooled to 450°C for 24 hr and then to 350°C for 24 hr, and held at 350°C for another 48 hr.

Another two set of Gd123ss samples were treated at 800°C and 200 ppm oxygen and 750°C and 30 ppm oxygen for various periods of time to study the reaction kinetics.

DTA was conducted using a Perkin-Elmer DTA 1700. A heating rate of 10°C/min and sample size of about 40mg were usually used. For very low oxygen partial

pressures, DTA was also conducted at a heating rate of 5°C/min to minimize the influence of oxygen released from the sample. The DTA temperatures were calibrated with the 808°C phase transition of $BaCO_3$ and the 1064°C melting of Au in nitrogen. A calibrated flow controller provided the purging gas of the required oxygen partial pressures at a flow rate of 100ml/min. Oxygen partial pressure was monitored by a zirconium oxide oxygen analyzer at the exhaust. Powder XRD was used to identify the phases. T_c's and hysteresis curves were measured by DC magnetic measurement with a Quantum Design MPMS SQUID system. Both the zero-field cooled curve and field cooled curve were measured with an applied field of 10 Oe. TEM was performed in a Philips C30 operated at 300 KeV.

2. Precipitation in Nd123ss

The lower solubility limits of Nd123ss in different P_{O_2} (oxygen, air, 1% and 0.1% oxygen) and temperatures (900°C to 20°C below the melting temperatures) were first determined by DTA and XRD lattice parameter measurement. The melt-texture growth of Nd123ss was conducted in a low Po_2 and then the samples were subjected to oxygen annealing to produce the precipitates. J_c will be determined from the hysteresis measurement. Microstructure will be studied by SEM and TEM.

Since our interest is the lower solubility limit, $Nd_{1+x}Ba_{2-x}Cu_3O_7$ with nominal compositions of $-0.20 \leq x \leq 0.10$ was studied. Nd123ss samples were prepared by a solid state reaction method. Appropriate amount of Nd_2O_3 (99.99%), $BaCO_3$ (99.997%) and CuO (99.995%) were mixed and calcined at 890-900°C in purified CO_2-free air flowing at 10 l/min for 24 hr three times with intermediate grindings. The grinding was

conducted in a micromill in a glovebox of dry nitrogen, which ensures a particle size of about 5 μm.

DTA was conducted in 1 bar, 0.2 bar, 0.01 bar and 0.001 bar Po_2 for the Nd123ss samples to determine approximately the eutectic temperatures and peritectic melting temperatures in these Po_2's. As maximum solubility is reported at the eutectic temperature between Nd123 and $BaCuO_2$ (011), Nd123ss samples were sintered at their respective eutectic temperatures for 48 hr to reach equilibrium conditions in the different Po_2's and then quenched. Another set of DTA's was then conducted for the sintered samples to better determine the thermal events in the different Po_2's. A Perkin-Elmer DTA 1700 was used for DTA measurements with a heating rate of 10°C/min, purging gas flow rate of 100 ml/min, and sample size of about 40 mg powder.

To determine the lower solubility limits, Nd123ss samples were pressed into pellets of about 0.2 g each and processed simultaneously at 900°C, around the eutectic temperatures, and 20°C below the peritectic temperatures in 1 bar, 0.2 bar, 0.01 bar and 0.001 bar Po_2, followed by quenching in the same atmosphere. To check whether equilibrium conditions have been reached for these samples, both forward reaction (synthesis) and back reaction (decomposition) were conducted for Nd123 in 1 bar Po_2 at 900°C for 48 hr. For the back reaction, a single phase Nd123 sample prepared in 0.01 bar Po_2 at 950°C was treated in 1 bar Po_2 at 900°C for 48 hr. As $BaCuO_2$ appears as a second phase from both directions, the equilibrium condition has been obtained. Since diffusion is faster in lower Po_2,[84,85] the holding time of 48 hr is adequate for the lower Po_2's. At higher temperatures, the holding time can be reduced. With a thermocouple attached to

the MgO single crystal substrate, the quench rate was measured at about 1000°C/min from the sintering temperature to 700°C and about 130°C/min from 700°C to 350°C. XRD analysis of the as-quenched samples showed scattering of lattice parameters due to differing amounts of oxygen uptake during quenching, depending on sample grain size and density. Therefore, it was necessary to anneal the samples in oxygen to obtain consistent oxygen content. However, the temperature of the oxygen annealing should be low enough to avoid second phase precipitation in the samples. It was shown that annealing at temperatures below 400°C for 100 hr will not affect the J_c-H curve significantly. Therefore, a 350°C and 48 hr oxygen annealing was first used and consistent results in lattice parameters for the samples treated in 1 bar Po_2 at 900°C were obtained. Unfortunately, this temperature is not high enough to fully oxygenate denser samples, even when the annealing time was increased to 100 hr. A 400°C, 48 hr oxygen annealing was used for all the other samples (Table 8).

XRD was conducted with a step size of 0.05°, collection time of 3 s, and 2θ from 20° to 120° for most samples. XRD was repeated for some samples with a step size of 0.02° and collection time of 8 s. The lattice parameters of the samples were obtained by a Rietveld refinement program (GSAS). The weighted residuals of the refinement are around 0.10-0.12, and the goodness of fit (χ^2) are around 2.0-4.0. Longer scans do give better precision, but the lattice parameters are unchanged.

For the melt-texture growth process, Nd123 precursor was pressed into a pellet of ~9.5 mm in diameter and ~10 mm in thickness. The pellet was placed on a flat single

Table 8 Experimental conditions and XRD results of $Nd_{1+x}Ba_{2-x}Cu_3O_7$

Composition x	a (Å)	b (Å)	c (Å)	V (Å^3)	Second phases
Treated at 1070°C in 1 bar Po_2 for 24 hr, annealed in 1 bar Po_2 at 350°C for 100hr					
-0.10	3.85886 (11)	3.91469 (14)	11.75933 (49)	177.639 (11)	011
-0.05	3.85832 (11)	3.91415 (14)	11.75882 (47)	177.582 (11)	011
0.00	3.85833 (10)	3.91494 (14)	11.75668 (49)	177.587 (10)	
0.05	3.85752 (11)	3.91394 (16)	11.74944 (43)	177.394 (10)	
0.10	3.85790 (10)	3.91040 (14)	11.74304 (48)	177.155 (10)	
Treated at 1030°C in 1 bar Po_2 for 36 hr, annealed in 1 bar Po_2 at 400°C for 48hr					
-0.20	3.85974 (13)	3.91393 (17)	11.76179 (58)	177.682 (14)	011
-0.15	3.85932 (13)	3.91374 (17)	11.76000 (58)	177.627 (14)	011
-0.10	3.85902 (13)	3.91350 (16)	11.76235 (52)	177.638 (13)	011
-0.05	3.85823 (10)	3.91415 (12)	11.75882 (44)	177.578 (10)	011
0.00	3.85843 (11)	3.91426 (14)	11.76014 (49)	177.612 (11)	
0.05	3.85743 (15)	3.91470 (24)	11.74962 (56)	177.427 (13)	
0.10	3.85878 (13)	3.90776 (16)	11.74703 (54)	177.136 (14)	
Treated at 900°C in 1 bar Po_2 for 48 hr, annealed in 1 bar Po_2 at 350°C for 48hr					
-0.20	3.86146 (8)	3.91033 (9)	11.75692 (31)	177.524 (8)	011
-0.15	3.86079 (13)	3.91074 (16)	11.75706 (53)	177.514 (14)	011
-0.10	3.86050 (12)	3.91093 (15)	11.75756 (51)	177.517 (13)	011
-0.05	3.85974 (14)	3.91107 (17)	11.75955 (58)	177.519 (15)	011
0.00	3.85957 (8)	3.91131 (9)	11.75832 (31)	177.503 (8)	011
0.05	3.85977 (14)	3.91060 (16)	11.76046 (56)	177.513 (14)	
0.10	3.86161 (14)	3.90801 (17)	11.75624 (57)	177.416 (15)	
Treated at 1050°C in 0.2 bar Po_2 for 24 hr, annealed in 1 bar Po_2 at 400°C for 48hr					
-0.20	3.86067 (13)	3.91450 (16)	11.76257 (53)	177.763 (13)	011
-0.15	3.85979 (12)	3.91436 (15)	11.76070 (51)	177.687 (12)	011
-0.10	3.85947 (11)	3.91394 (15)	11.76167 (49)	177.669 (12)	011
-0.05	3.85913 (6)	3.91403 (8)	11.76277 (26)	177.674 (6)	011
0.00	3.85862 (6)	3.91396 (8)	11.76331 (26)	177.655 (7)	
0.05	3.85738 (11)	3.91391 (15)	11.75173 (55)	177.421 (11)	
0.10	3.85784 (10)	3.91102 (14)	11.74367 (48)	177.190 (10)	
Treated at 998°C in 0.2 bar Po_2 for 48 hr, annealed in 1 bar Po_2 at 400°C for 48hr					
-0.20	3.85863 (13)	3.91319 (15)	11.76131 (52)	177.591 (13)	011
-0.15	3.85900 (11)	3.91358 (14)	11.75968 (49)	177.601 (12)	011
-0.10	3.85863 (11)	3.91322 (14)	11.75943 (48)	177.564 (12)	011
-0.05	3.85860 (12)	3.91323 (14)	11.76078 (49)	177.583 (12)	011
0.00	3.85838 (10)	3.91391 (13)	11.76001 (45)	177.592 (10)	
0.05	3.85707 (15)	3.91358 (21)	11.74880 (47)	177.347 (14)	
0.10	3.85977 (12)	3.90759 (15)	11.74809 (51)	177.189 (13)	
Treated at 900°C in 0.2 bar Po_2 for 48hr, annealed in 1 bar Po_2 at 350°C for 48hr					
-0.20	3.86124 (14)	3.91035 (17)	11.75813 (57)	177.533 (15)	011
-0.15	3.86153 (12)	3.91119 (15)	11.75722 (50)	177.572 (13)	011
-0.10	3.86064 (12)	3.91085 (14)	11.75955 (50)	177.550 (13)	011
-0.05	3.85928 (12)	3.91118 (15)	11.75885 (49)	177.492 (13)	011
0.00	3.85988 (12)	3.91138 (15)	11.76063 (49)	177.555 (13)	011
0.05	3.85908 (13)	3.91048 (15)	11.75953 (46)	177.461 (13)	
0.10	3.85977 (13)	3.90743 (15)	11.75416 (50)	177.274 (13)	

Table 8 (continued)

Composition x	a (Å)	b (Å)	c (Å)	V (Å^3)	Second phases
Treated at 1010°C in 0.01 bar Po_2 for 36hr, annealed in 1 bar Po_2 at 400°C for 48hr					
-0.20	3.85993 (12)	3.91462 (16)	11.76071 (51)	177.707 (13)	011
-0.15	3.85908 (12)	3.91402 (16)	11.76110 (53)	177.646 (13)	011
-0.10	3.85952 (11)	3.91443 (14)	11.75933 (49)	177.658 (11)	
-0.05	3.85877 (14)	3.91417 (17)	11.76160 (61)	177.646 (14)	
0.00	3.85829 (10)	3.91410 (12)	11.76119 (42)	177.614 (10)	
0.05	3.85679 (9)	3.91375 (13)	11.75107 (47)	177.377 (10)	
0.10	3.85672 (12)	3.91312 (17)	11.74882 (45)	177.311 (12)	422
Treated at 937°C in 0.01 bar Po_2 for 48hr, annealed in 1 bar Po_2 at 400°C for 48hr					
-0.20	3.86006 (13)	3.91208 (16)	11.76378 (53)	177.643 (14)	011
-0.15	3.85995 (13)	3.91252 (16)	11.76295 (52)	177.645 (13)	011
-0.10	3.85979 (12)	3.91335 (15)	11.76151 (50)	177.654 (12)	011
-0.05	3.85942 (10)	3.91362 (13)	11.76236 (43)	177.663 (11)	
0.00	3.85873 (10)	3.91317 (12)	11.76485 (42)	177.647 (11)	
0.05	3.85743 (9)	3.91363 (15)	11.74933 (52)	177.374 (10)	
0.10	3.85947 (10)	3.90888 (13)	11.74447 (43)	177.179 (10)	
Treated at 900°C in 0.01 bar Po_2 for 48hr, annealed in 1 bar Po_2 at 400°C for 48hr					
-0.20	3.86073 (15)	3.91471 (22)	11.75842 (70)	177.713 (16)	011
-0.15	3.85974 (11)	3.91376 (14)	11.76003 (49)	177.648 (12)	011
-0.10	3.86001 (10)	3.91437 (14)	11.75879 (47)	177.670 (11)	011
-0.05	3.85971 (10)	3.91416 (13)	11.76064 (45)	177.674 (11)	011
0.00	3.85873 (10	3.91360 (12)	11.76089 (43)	177.607 (10)	
0.05	3.85753 (10)	3.91350 (15)	11.74976 (53)	177.380 (11)	
0.10	3.86029 (12)	3.90823 (15)	11.74761 (50)	177.235 (12)	
Treated at 990°C in 0.001 bar Po_2 for 48hr, annealed in 1 bar Po_2 at 400°C for 48hr					
-0.20	3.85950 (22)	3.91444 (28)	11.75951 (97)	177.660 (22)	422, unidentified
-0.15	3.85903 (17)	3.91444 (22)	11.76060 (76)	177.655 (18)	422, unidentified
-0.10	3.85926 (17)	3.91384 (22)	11.76185 (72)	177.657 (18)	422, unidentified
-0.05	3.85926 (17)	3.91324 (20)	11.76162 (61)	177.627 (16)	422, unidentified
0.00	3.85808 (11)	3.91360 (14)	11.76085 (49)	177.576 (12)	
0.05	3.85663 (13)	3.91363 (17)	11.75650 (61)	177.446 (14)	422
0.10	3.85682 (17)	3.91228 (22)	11.75727 (61)	177.405 (16)	422, unidentified
Treated at 915°C in 0.001 bar Po_2 for 48hr, annealed in 1 bar Po_2 at 400°C for 48hr					
-0.20	3.85999 (7)	3.91416 (9)	11.75978 (29)	177.674 (7)	422, 011
-0.15	3.85959 (11)	3.91404 (15)	11.75940 (49)	177.644 (12)	011
-0.10	3.85966 (11)	3.91452 (15)	11.75810 (52)	177.650 (12)	
-0.05	3.85901 (10)	3.91418 (13)	11.75993 (44)	177.632 (10)	
0.00	3.85888 (11)	3.91359 (13)	11.76251 (44)	177.638 (11)	
0.05	3.85717 (9)	3.91326 (13)	11.75141 (44)	177.377 (9)	
0.10	3.85803 (12)	3.90867 (14)	11.75026 (47)	177.191 (12)	
Treated at 900°C in 0.001 bar Po_2 for 48hr, annealed in 1 bar Po_2 at 400°C for 48hr					
-0.20	3.86055 (16)	3.91285 (19)	11.76244 (65)	177.681 (16)	011
-0.15	3.85980 (14)	3.91302 (18)	11.76331 (59)	177.667 (15)	011
-0.10	3.85995 (13)	3.91371 (16)	11.75924 (53)	177.644 (13)	
-0.05	3.85948 (12)	3.91391 (15)	11.76041 (51)	177.649 (12)	
0.00	3.85896 (12)	3.91361 (15)	11.76264 (52)	177.645 (13)	
0.05	3.85752 (10)	3.91354 (14)	11.75170 (49)	177.410 (10)	
0.10	3.85950 (14)	3.90736 (17)	11.74777 (51)	177.162 (14)	

crystal MgO for melt processing. A purging gas of 500 ppm oxygen in nitrogen, at a total pressure of 1 bar, was chosen to alleviate the substrate reaction. The sample was heated to 1015°C at a heating rate of 10°C/min, held at that temperature for 0.5 h, cooled down to 920°C at 0.01°C/min, then furnace cooled. The prepared sample consists of well-textured domains of Nd123. Powder XRD revealed that the sample is composed of Nd123 with a minor amount of Nd422. Microprobe analysis with a sintered Nd123 standard verified that the Nd123 phase has the stoichiometric composition within an experimental error of 3%. The sample was crushed into small pieces with the cleaved shining surface of a-b plane as the broad surface. These small pieces (side 0.2-1.5 mm, thickness 0.1-0.3 mm) were subject to three different oxygen annealing: 350°C for 96 hr, 500°C for 96 hr followed by 350°C for 96 hr, 900°C for 48 hr followed by 350°C for 96 hr.

A sample with a starting composition of x = -0.1 was also prepared in the same way.

SEM was performed in a Cambridge 200 SEM machine. For TEM, a sample was crushed in a mortar into small crystals suspended in ethanol. These small crystals were floated onto a gold mesh for TEM observation in a Philips C30 operated at 300 KeV.

CHAPTER IV RESULTS AND DISCUSSION

1. Precipitation in Gd123ss

A. Choice of processing parameters

Figure 13 shows the stability range of Gd123 determined by DTA and XRD. In order to maintain superconductivity, Gd123ss can only be treated within the stability range of Gd123. Since extra oxygen is required in Gd123ss than in Gd123, the Gibbs free energy curve of the solid solution may become steeper in lower Po_2. Depending on the change of the Gibbs free energies of other phases, a lower Po_2 may provide a higher driving force for decomposition of the solid solution. However, as the Po_2 decreases, the temperature limit for stable Gd123 phase also decreases. At very low oxygen partial pressure, the allowable processing temperature may be so low that the kinetics for precipitation may also be very slow. Therefore, oxygen partial pressures of 300 ppm and 30 ppm (Commercial nitrogen gas) were chosen for the processing of Gd123ss.

The size of the second phase is an important consideration for the enhancement of J_c. In order to obtain a fine second phase, solid state decomposition is desired. As Gd_2BaCuO_5 (211) and CuO precipitate from Gd123ss, a liquid is formed at high temperature. It is necessary to treat the material below the liquid formation temperature to avoid excess coarsening of the second phases. Therefore, the liquid formation temperatures were further determined by DTA, as shown in Figure 14. As a result, 800-870°C were used in 300 ppm Po_2 and lower temperatures of 700-800°C were used in 30 ppm Po_2.

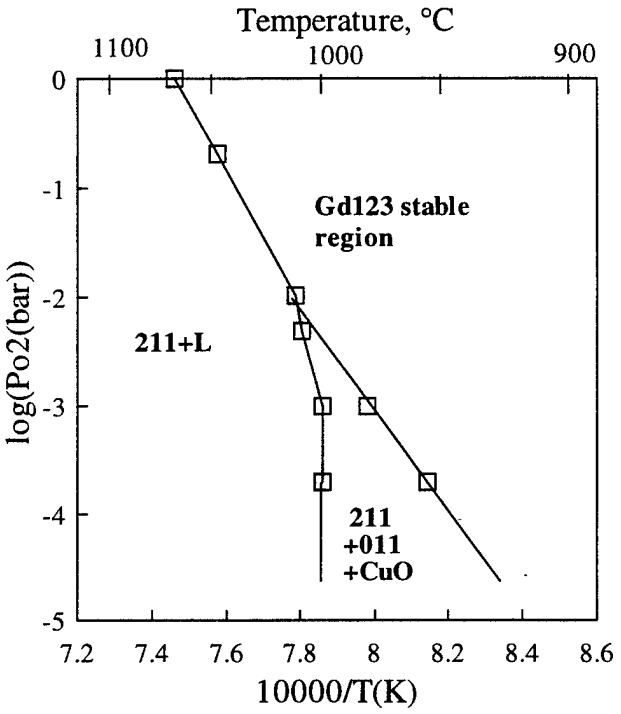

Figure 13 Stability range of Gd123.[44]

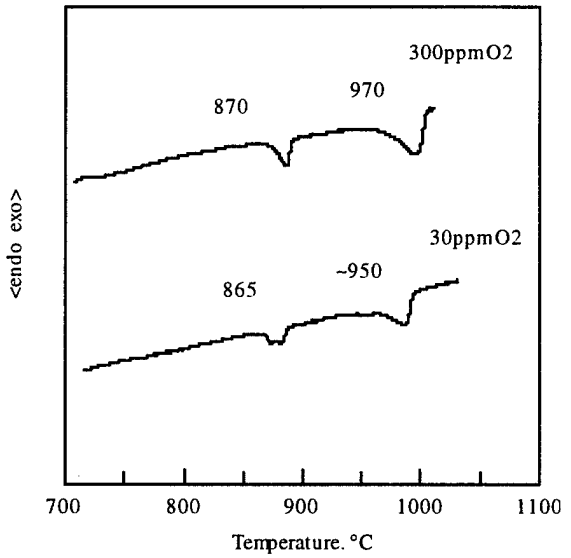

Figure 14 Liquid formation temperature of Gd123ss (x=0.2) by DTA.[44]

B. Effects of decomposition of Gd123ss

Figure 15 compares the XRD patterns of Gd123ss before and after different decomposition treatments. Except for the sample treated at 700°C in 30ppm O_2, all the samples show 211 phase precipitated from the single phase starting material. The line broadening of the 211 phase for the lower temperatures indicates the small size of this phase. The peak for CuO at 2θ = 35.6 is not that obvious for all samples except the sample treated at 870°C. However, there should be a Cu-rich phase in order to maintain mass balance.

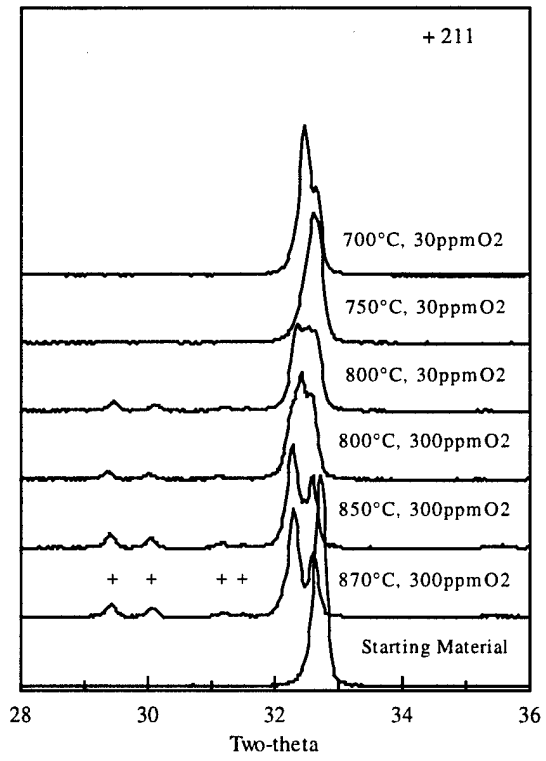

Figure 15 XRD of Gd123ss starting material and after decomposition for 24 hr.[44]

As shown in Figure 16, T_c increases as a result of the decomposition of the solid solution. For all the samples treated at 750°C or above, T_c onsets have reached the value of Gd123. This suggests that equilibrium composition for these conditions will be very close to Gd123. The broad transitions show the progress of the decomposition process. Given enough time, more precipitation will occur. Even the sample treated at 700°C in 30ppm O_2 show increase in T_c due to decomposition although XRD cannot detect any second phases. The small values of field cooled magnetization indicate flux pinning in the samples.

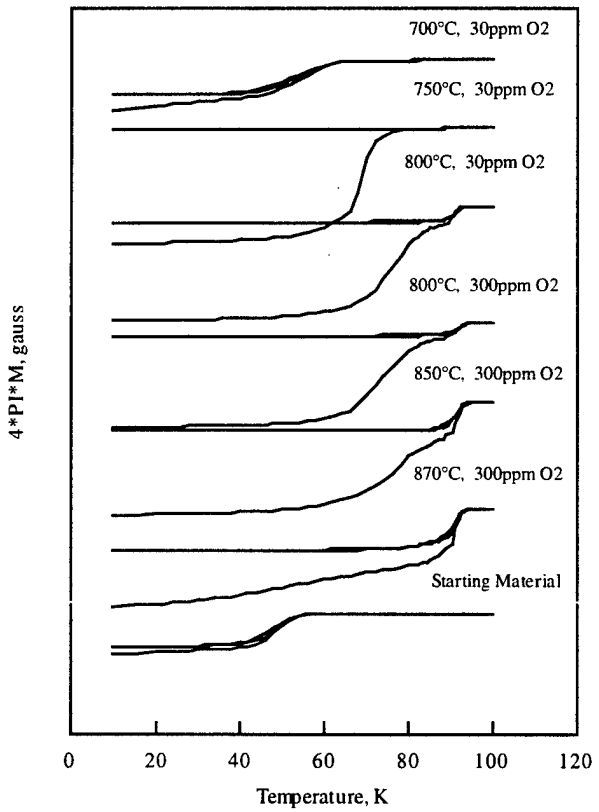

Figure 16 T_c of Gd123ss before and after decomposition treatment.[44]

Figure 17 is the magnetization hysteresis (ΔM) measured at 10K for Gd123ss samples after decomposition. For the same Po_2, ΔM increases with the processing temperature. For the same temperature, ΔM increases with decreasing Po_2. As SEM shows certain grain growth only for the sample treated at 870°C in 300ppm O_2, other samples have similar grain size as the starting material. The increase in the magnetization hysteresis indicates enhancement of J_c due to second phases. With an average grain size of 5 μm, the peak value can be estimated at about $5x10^6$ A/cm^2. However, the enhancement of J_c is not optimal in the current processing condition. On one hand, the decomposition is not complete, especially for the samples treated at lower temperatures, therefore, the full potential of dispersed second phases has not been reached. On the other hand, the small grain size makes it difficult to assess the flux pinning performance at high temperature of 77 K as the background magnetization of Gd^{3+} is strong. It was suspected that the low density and small grain size would make surface and grain boundary decomposition substantial. Such surface precipitation is not beneficial to flux pinning, and even worse, it creates grain boundary weaklink. Later, TEM shows that surface and grain boundary are not preferential nucleation sites in this system.

Figure 18 shows the change of T_c for Gd123ss ($x = 0.2$) samples treated at 800°C in 200 ppm O_2 and 750°C in 30 ppm O_2 for different periods of time. There is a slow transformation period at the beginning. This may be caused partially by the time required to obtain the low oxygen content inside the grains. The transformation is much faster at 800° in 200 ppm O_2 than at 750°C in 30 ppm O_2. Therefore, temperature is a more

effective parameter to control the transformation kinetics. There seem to be two plateaus in the magnetization curves, indicating two superconducting phases. However, the amount of second phases cannot be accurately determined and quantitative analysis was not conducted.

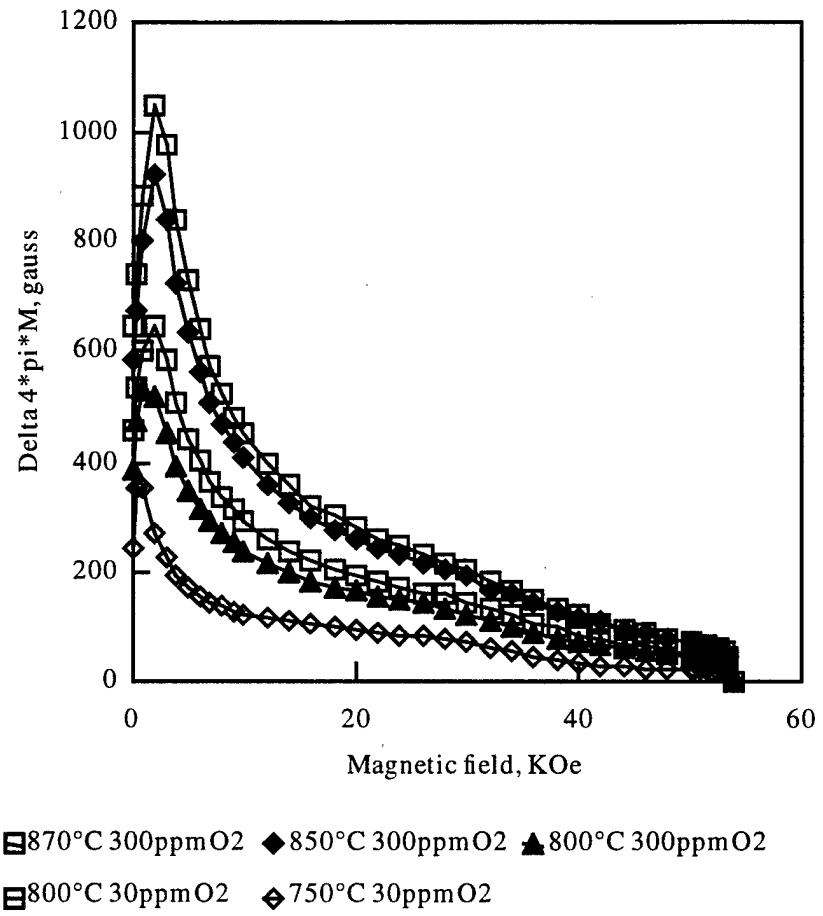

Figure 17 Magnetization hysteresis of Gd123ss at 10 K after decomposition in low oxygen partial pressures for 24 hr.[44]

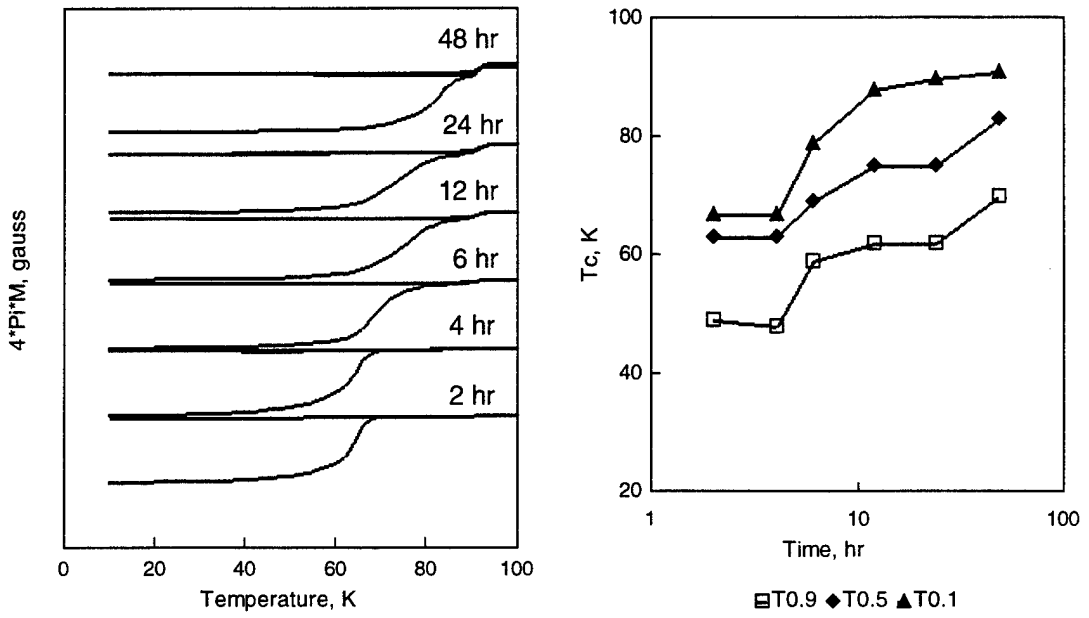

(a)

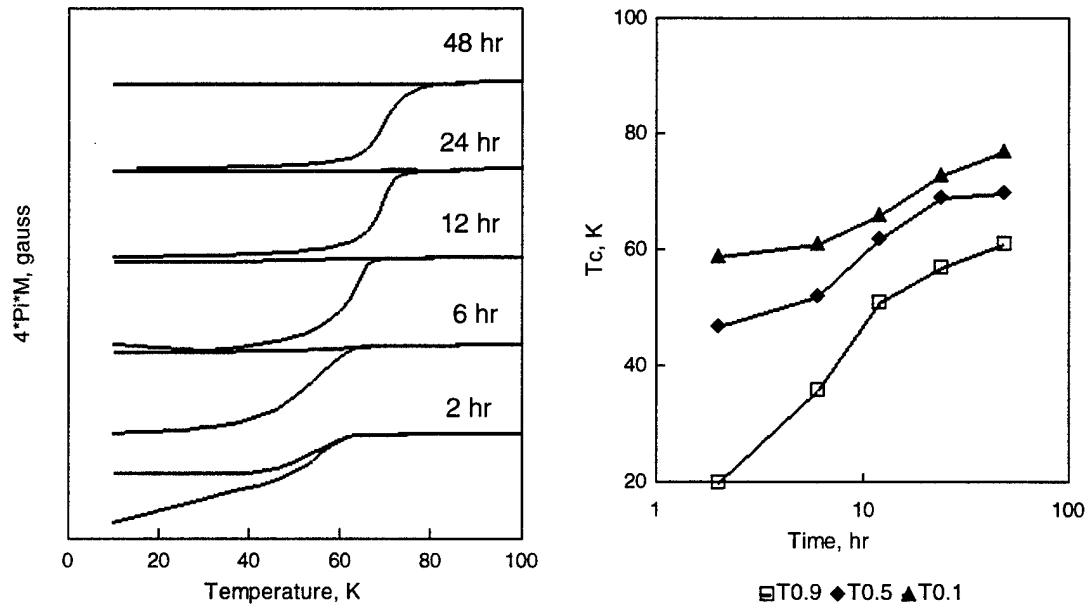

(b)

Figure 18 Tc of Gd123ss treated at (a) 800°C in 200 ppm O_2 and (b) 750°C in 30 ppm O_2 for different periods of time. $T_{0.9}$, $T_{0.5}$, and $T_{0.1}$ are the temperatures for 90%, 50% and 10% of the magnetization values at 10K respectively.

C. Microstructure

To understand the precipitation mechanism, microstructure analysis was conducted for the samples. Figure 19 is the optical micrograph of a sample treated at 800°C in 200 ppm oxygen for 24 hr. The tiny black spots in the micrograph are of blue color under polarized light. These are particles of Gd211 precipitate with a size less than 0.5 μm. They seem to nucleate both inside the grain and along the grain boundary. Therefore, grain boundaries are not the preferential nucleation sites. However, the particle density is very low, only about one to three Gd211 particles in the cross section of each grain. With the precipitation of Gd211, CuO or some other Cu-rich phase should also exist as required by mass balance. However, no such phase was observed in the optical micrography.

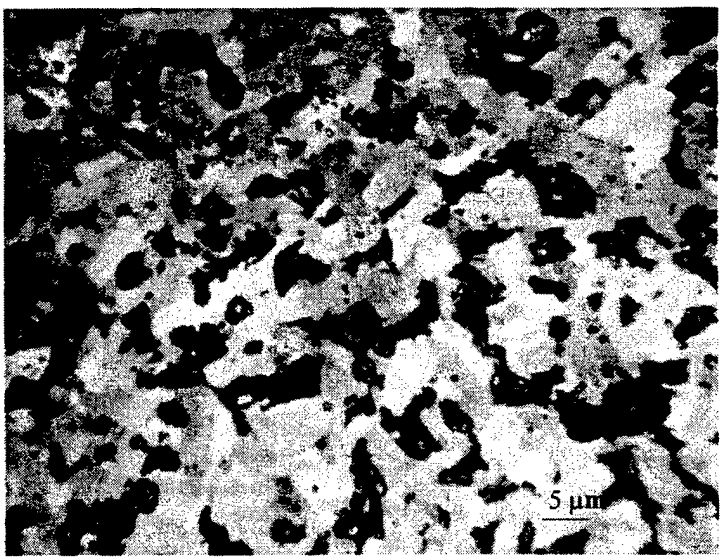

Figure 19 Optical micrography of Gd123ss under polarized light. Second phase is seen as tiny dark spots. The different shades of gray are caused by the orientation of the Gd123ss phase. The black regions are pores filled with epoxy in order to retain possible precipitates on surfaces.

TEM was conducted to further identify the precipitates. Figure 20 shows a spherical Gd211 particle inside the grain. No other second phases are detected immediately around this precipitate. The selected area diffraction pattern does not show any special orientation relationship between the precipitate and the matrix (Figure 21). Whether there is an orientation relationship during the nucleation stage requires further research.

Lots of stacking faults are observed in the matrix (Figure 22). It is common to observe some 124-type stacking faults in Y123 samples, where an extra CuO layer is inserted between the123 unit cells. In the precipitation process of Gd123ss, there must be some CuO-rich phase along with the formation of Gd211. Therefore, it is very likely that the stacking faults are of 124 type.

From the T_c plateau around 80 K in Figure 18, it is even possible that some Gd124 phase is formed during the treatment at 800°C in 200 ppm oxygen. In Y-Ba-Cu-O system, Y124 is stable at ambient pressure below some 850°C.[19] It has a nearly constant oxygen content as $YBa_2Cu_4O_8$ and a transition temperature around 80 K. As oxygen is released during its decomposition into 123, its thermal stability is decreased in low oxygen partial pressures. The stability of Gd124 is perhaps similar to that of Y124. Most of the work on the 124 phase deals with the phase stability and phase relations in high oxygen partial pressures. The stability data of 124 phase in low Po_2 is not available. If Gd124 is not a stable phase at the processing condition, it may be formed as a metastable phase due to the lower interface energy. It is also not known whether a solid solution is formed between Gd and Ba in the 124 phase.

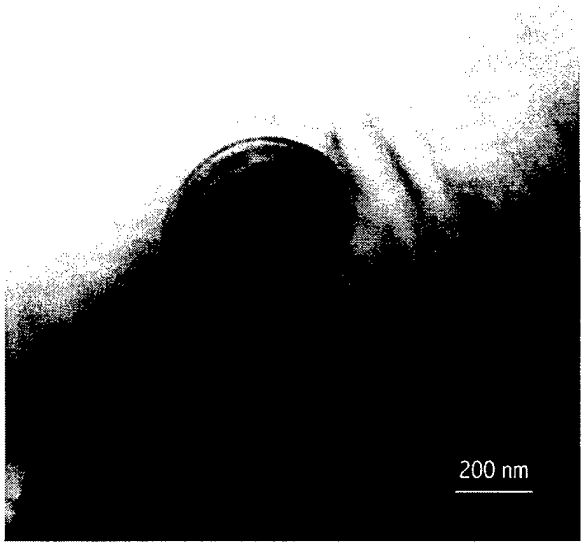

Figure 20 TEM shows the spherical Gd211 phase.

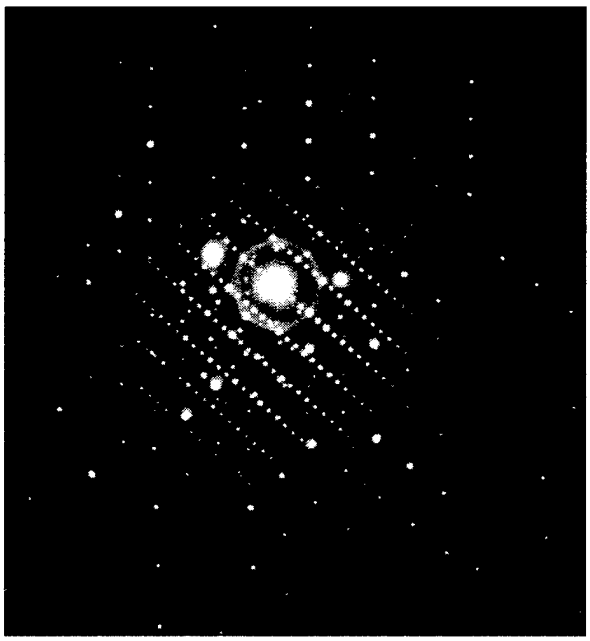

Figure 21 Selected area diffraction pattern of Gd123ss and Gd211.

Figure 22 TEM of stacking faults. Twins and a grain boundary are also shown.

The nucleation density of Gd211 phase is very low while the size of the precipitate is big. At present, we do not have enough data for the calculation of the nucleation rate but we can do a rough estimate of the diffusion distance for the sample treated at 800°C in 200 ppm O_2 for 24 hr. Suppose the precipitation has proceeded to the matrix composition of x ~ 0.08, we will have ~10% volume of Gd211 phase. For the formation of a particle of 0.5 μm, the diameter of the original Gd123ss phase should be ~1.5 μm. Therefore, the diffusion distance is around 0.5 μm from the particle surface. Suppose the diffusion coefficient of Gd is around 10^{-18} cm^2s^{-1},[47] we will get a diffusion distance of $\sqrt{6Dt} = \sqrt{6 \cdot 10^{-18} \cdot 24 \cdot 3600} = 7x10^{-7}$ cm = 0.007 μm. The actual diffusion distance is about two orders of magnitude higher. That is equivalent to a diffusion

coefficient that is four orders of magnitude higher. Perhaps the stacking faults and the associated partial dislocations provide a short cut of diffusion.

Another concern is that whether the precipitation takes place preferentially along the grain boundaries. TEM shows that the grain boundaries are clean (Figure 23). Therefore, it is possible to obtain the enhanced flux pinning from precipitates and maintain the grain boundaries free of weaklinks.

In comparison with the decomposition of Y124, Gd123ss has the potential to be prepared by existing processing methods that can overcome the grain boundary weaklinks. The 124 phase will decompose into 123 plus CuO at high temperature. It is

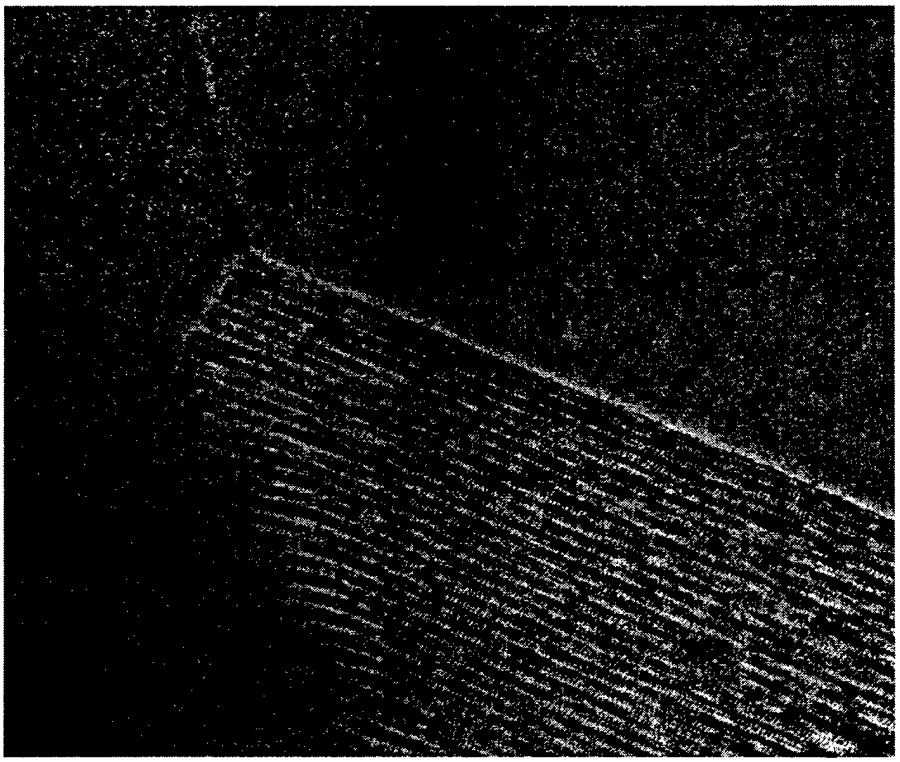

Figure 23 Lattice image of grain boundaries in Gd123ss treated at 800°C in 200 ppm O_2. The grain at the upper right corner is Gd211.

not possible to use the melt-texture process or other liquid assisted processing methods to make textured 124 phase. As for Gd123ss (x = 0.2), it may be prepared by the melt-texture growth process. Since the highest melting temperature in Gd123ss is around the stoichiometric composition, the usual melt-texture process of continuous slow cooling will produce a Gd123ss very close to the stoichiometric composition. A special process needs to be developed to obtain a textured supersaturated Gd123ss in order to carry out the precipitation reaction. One way is to conduct the melt-texture process at a lower temperature so that Gd123ss with larger x can also have a chance of formation. High temperature sintering near the melting point of Gd123ss (say x = 0.2) may be another option.

2. Precipitation in Nd123ss

A. Lower solubility limit of Nd123ss

Figure 24 shows the DTA curves of Nd123ss in 1 bar, 0.2 bar, 0.01 bar and 0.001 bar Po_2. The large endothermic peaks at high temperatures correspond to the peritectic melting of Nd123ss while small endothermic peaks appear at lower temperatures for compositions beyond the lower solubility limits. For compositions within the solid solution range, the large endothermic peaks are the peritectic melting temperatures of the corresponding solid solutions in the specified Po_2's. The measured decomposition temperatures for x = 0 are 5-10°C higher than the results of Lindemer et al.[86] in 0.01 bar and 0.001 bar Po_2, but about 10°C lower in 1 bar Po_2. The decomposition temperatures in 0.2 bar Po_2 for $x \geq 0$ are about 10°C higher than those reported by Osamura and

Zhang[33] and are in good agreement with the predictions of Lindemer et al..[86] For compositions beyond the solid solubility limits, Nd123ss of these compositions do not exist and the peaks are the peritectic melting of the solid phases in equilibrium with these compositions. The small shoulder on these peaks may be due to the formation of the Nd422 phase at high temperatures.

The small endothermic peaks at low temperatures are considered by Osamura and Zhang as the results of the peritectic reaction between 123 and 011 to form Nd422 phase and liquid (Figure 8).[33] However, Nd422 phase is not observed for the samples quenched from these temperatures in 0.01 to 1 bar Po_2 (Table 8). Unlike the 011 phase which may melt at high temperature and obtain a fine size during quench, Nd422 phase formed at the peritectic temperature must have a big grain size and thus is easy to detect by XRD. The lack of Nd422 phase suggests that a eutectic reaction is responsible for the small peaks and the peritectic reaction happens at higher temperatures at which the Nd422 phase is formed.

The appearance of small endothermic peaks at lower temperature indicates that the composition is beyond the solid solubility limit in the particular Po_2. In 1 bar and 0.2 bar Po_2, the DTA curves show double peaks for $x < -0.05$ (Figure 24 a and b). The first peak is believed to be caused by the solubility change with temperature, and the second peak, much larger, is the eutectic reaction between Nd123ss and $BaCuO_2$ to form a liquid phase. In 0.01 bar and 0.001 bar Po_2 (Figure 24 c and d), the first peak disappears, consistent with little solubility change in lower Po_2's as determined by the XRD results below.

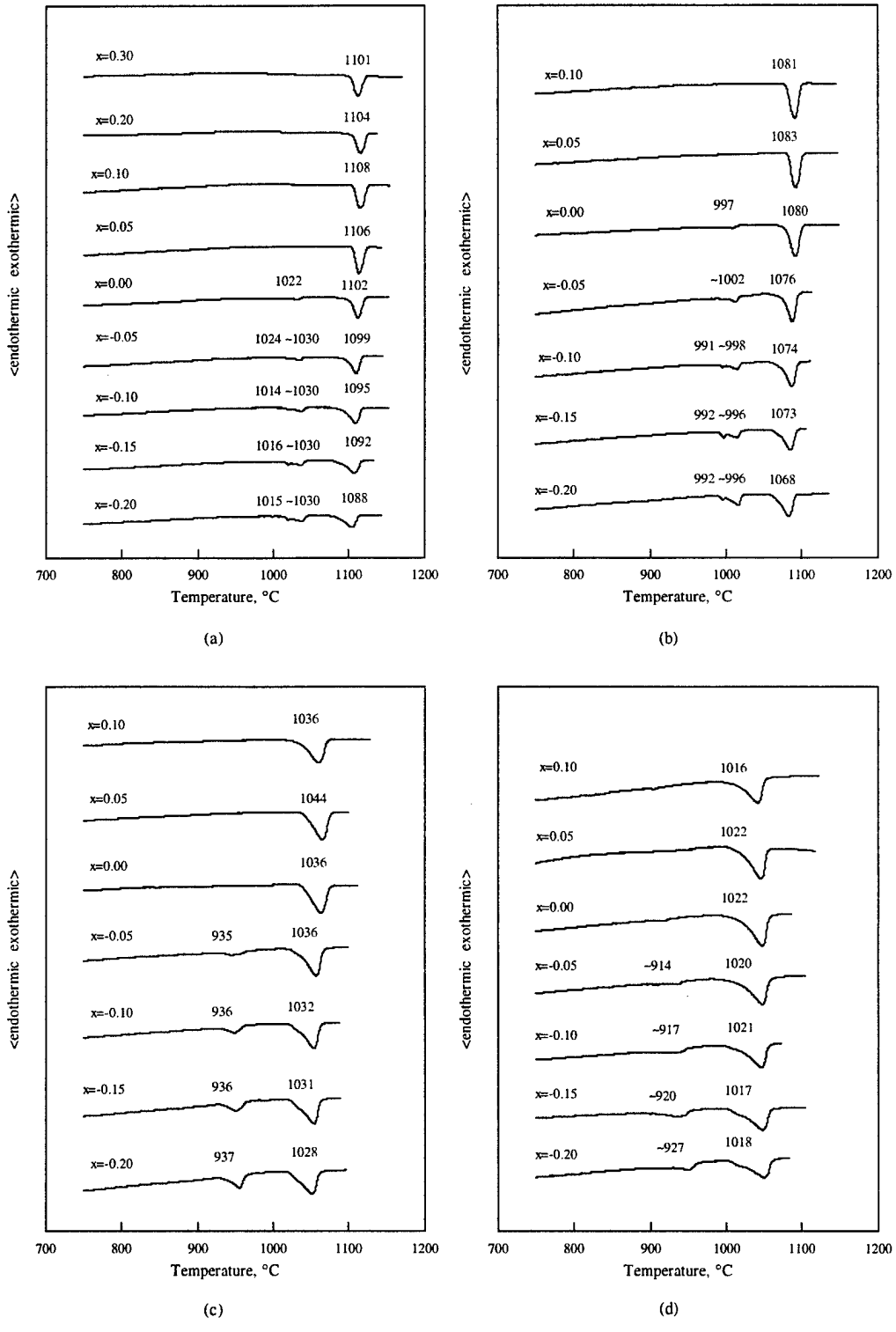

Figure 24 DTA of Nd123ss in (a) 1 bar Po_2, (b) 0.2 bar Po_2, (c) 0.01 bar Po_2, and (d) 0.001 bar Po_2.[87]

In Figure 25, we normalize the melting temperatures of Nd123ss samples against the maximum melting temperatures in each Po_2. As stated above, the data points for compositions beyond the solid solubility limits are not the melting temperatures of the solid solution of that composition, but they may reveal the slope of the solubility curve in the phase diagram. In 0.001 bar Po_2, there is little change of the melting temperatures for $x < 0.05$, implying a relatively sharp slope of the solid solubility curve below the melting temperature. However, the melting temperature cannot be measured very accurately as the shoulder peak of 422 formation will affect the measurement of the onset position of the peak. For compositions on the solid solution side, the melting temperatures represent the relative stability of the corresponding solid solutions. We can see that in 1 bar Po_2 the stability changes slowly with x while the stability drops faster with decreasing Po_2. Therefore, sintering of Nd123 in a low Po_2 tends to result in a sharp superconducting transition because Nd123ss's with compositions of large x are much less stable. In 1 bar and 0.2 bar Po_2, a wide range of solid solutions is often encountered, giving a broad transition.[28] In 1 bar and 0.2 bar Po_2, sharp transitions can only be achieved after long sintering time at high temperature. For the same reason, melt-texture growth of Nd123 in 1 bar and 0.2 bar Po_2 produces broad transitions while in 0.01 bar and 0.001 bar Po_2 sharp transitions are achieved.[9,88]

It is also noticed that the maximum melting temperatures do not occur at the stoichiometric composition, instead they shift to larger x in higher Po_2's. In 1 bar Po_2, the maximum melting temperature corresponds to the composition of $x = 0.10$. In lower Po_2's, the maximum melting temperatures occur at a lower value of $x \sim 0.05$. From the

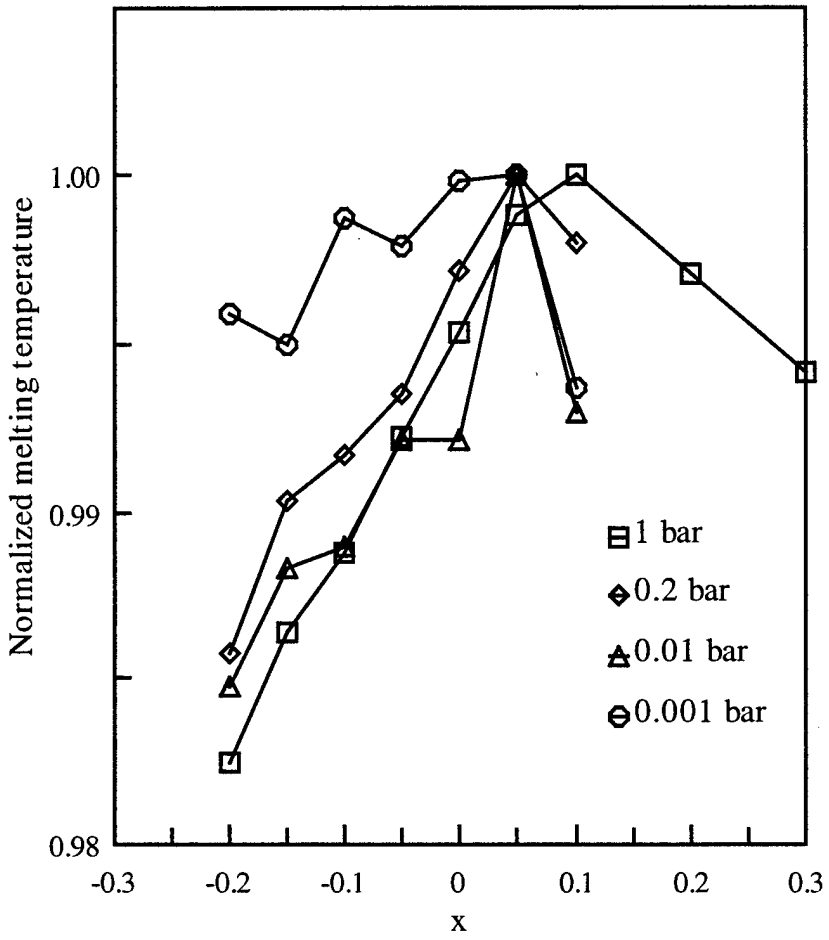

Figure 25 Normalized melting temperatures of Nd123ss in 1 bar, 0.2 bar, 0.01 bar and 0.001 bar Po_2.[87]

XRD measurement below, we can determine more precisely that the maximum melting temperature occurs at x = 0.00 in 0.001 bar Po_2 since samples on both sides treated at 990°C show second phases. The solid solubility of a compound may be treated by the sublattice model. For example, Li et al.[89] successfully calculated the solid solution range of AlLi based on the sublattice model. It is found that the energy associated with one kind of atom substituted into another sublattice plays an important role. Not only is the

solid solution range biased towards the lower energy side, but also the most stable composition shifts in the same direction.[89] Nd123ss is much more complicated since more sublattices are involved. Nevertheless, as the energy for Nd^{3+} to substitute for Ba^{2+} is much lower than that for Ba^{2+} in the Nd^{3+} lattice, solid solution is predominantly in the Nd-rich side, and the most stable composition shifts accordingly. As Nd^{3+} substitution into the Ba^{2+} sublattice also introduces oxygen into the oxygen sublattice, lower Po_2 will not favor such a substitution. Therefore, the most stable composition moves closer to the stoichiometric composition. However, in contrast to what is expected, the upper solid solubility is not affected much by the Po_2.[90,34] Extensive solid solution ranges also exist for other phases (Nd422, Nd201) in this system.[33] The Gibbs free energy of these phases may also change with Po_2 in such a way that the upper solubility limit of Nd123ss does not significantly change.

The above analysis is verified by a recent result of Nd123ss single crystals fabricated by the top-seeded solution-growth method in oxygen, air and 1% oxygen.[91] The same Ba-Cu-O solvent with a Ba/Cu ratio of 3:5 was used in a Nd_2O_3 crucible for all the samples. In such a growth condition, it is expected that the composition of the crystal will correspond to the most stable composition in that Po_2. The compositions (Nd:Ba:Cu) of the single crystals are 1.10:1.90:3.00 in oxygen, 1.07:1.95:3.00 in air, and 1.01:1.97:3.00 in 1% oxygen. The superconducting transition temperatures are 88 K, 92 K and 96 K respectively.

To determine the lower solubility limits more precisely, the changes in lattice parameters and unit cell volume with composition were measured. Figure 26-Figure 29

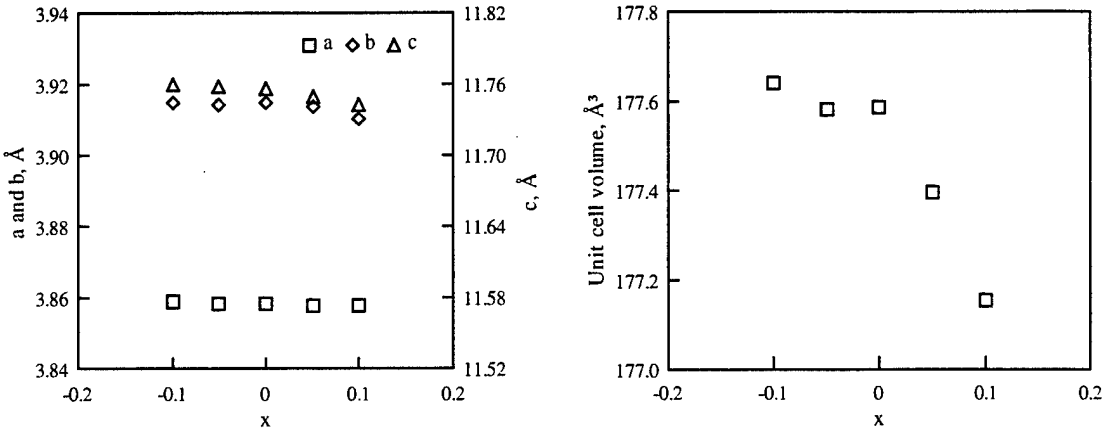

(a)

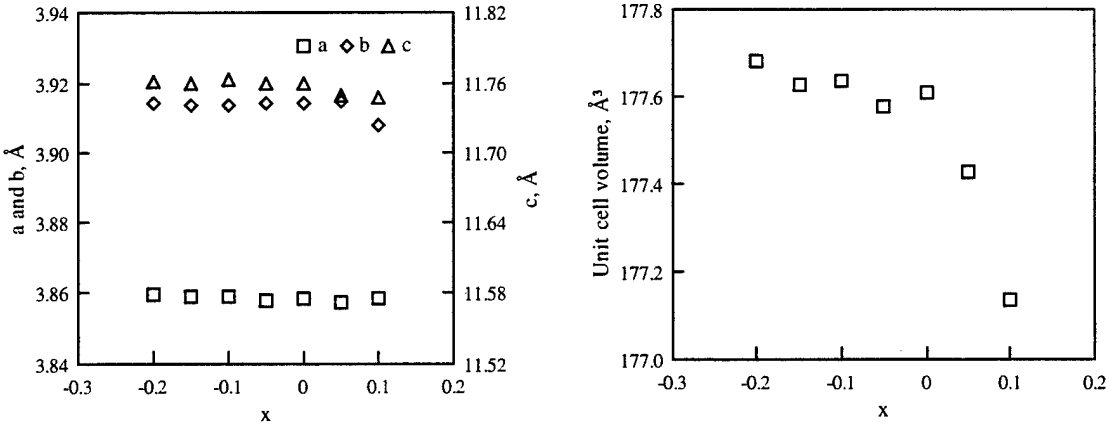

(b)

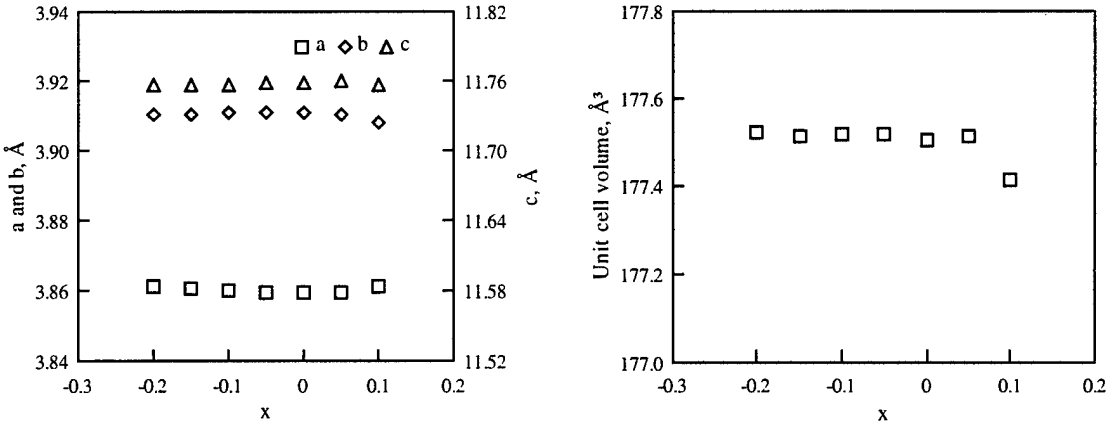

(c)

Figure 26 Lattice parameters and unit cell volume of Nd123ss treated in 1 bar Po_2 at (a) 1070°C, (b) 1030°C and (c) 900°C.[87]

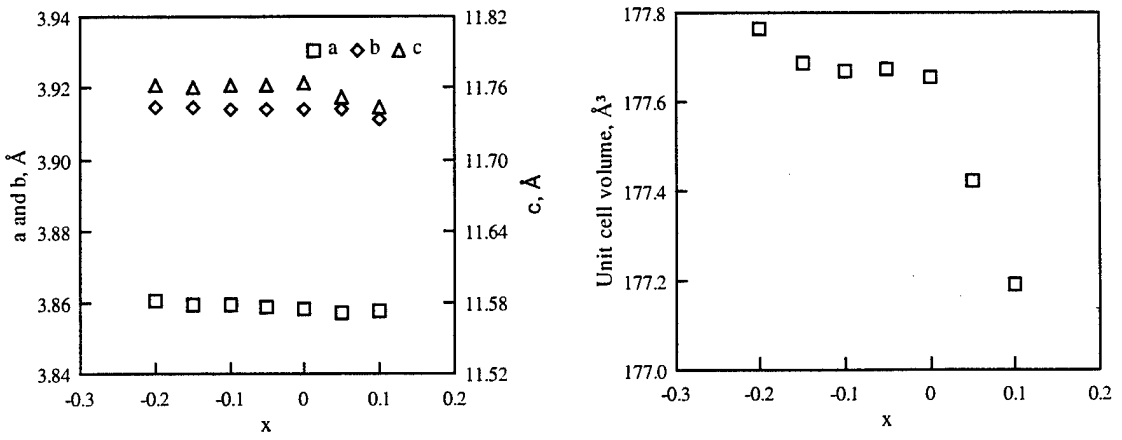

(a)

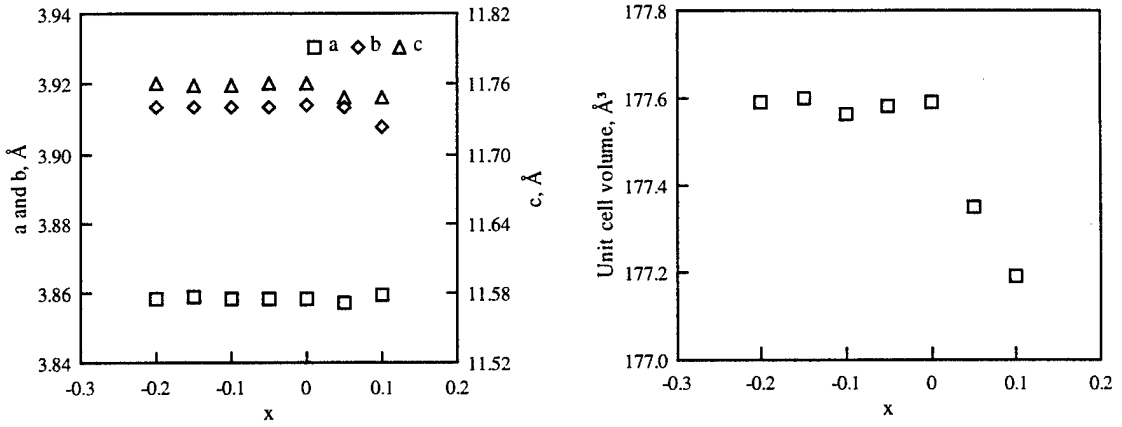

(b)

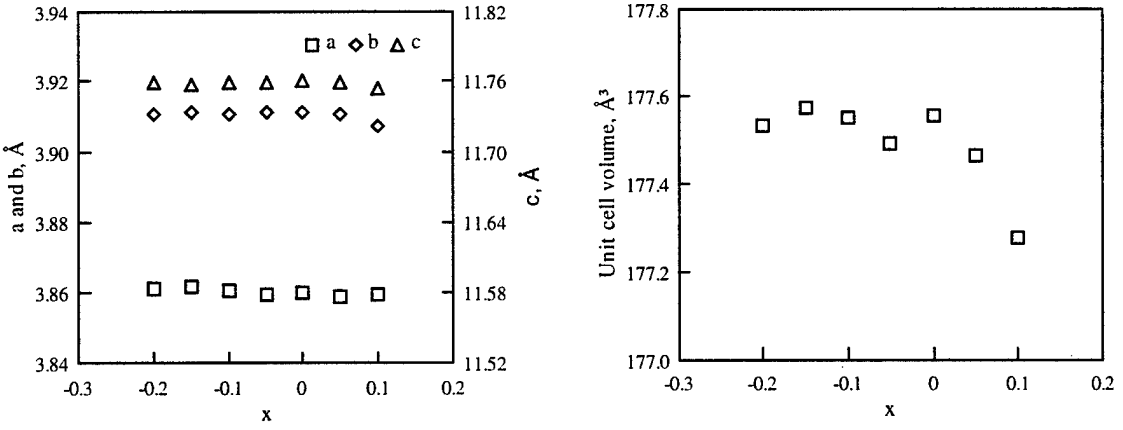

(c)

Figure 27 Lattice parameters and unit cell volume of Nd123ss treated in 0.2 bar Po_2 at (a) 1050°C, (b) 998°C and (c) 900°C.[87]

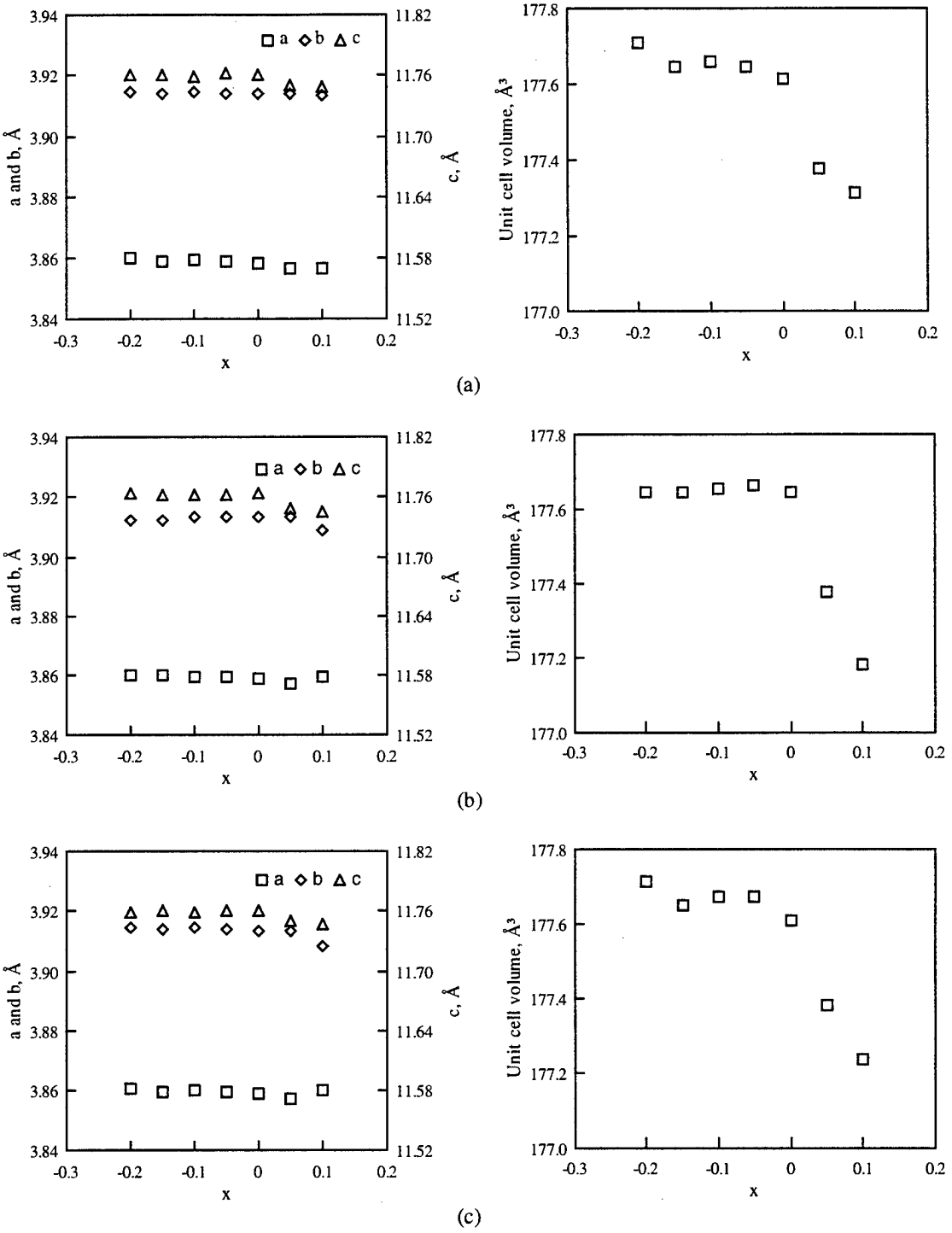

Figure 28 Lattice parameters and unit cell volume of Nd123ss treated in 0.01 bar Po_2 at (a) 1010°C, (b) 937°C and (c) 900°C.[87]

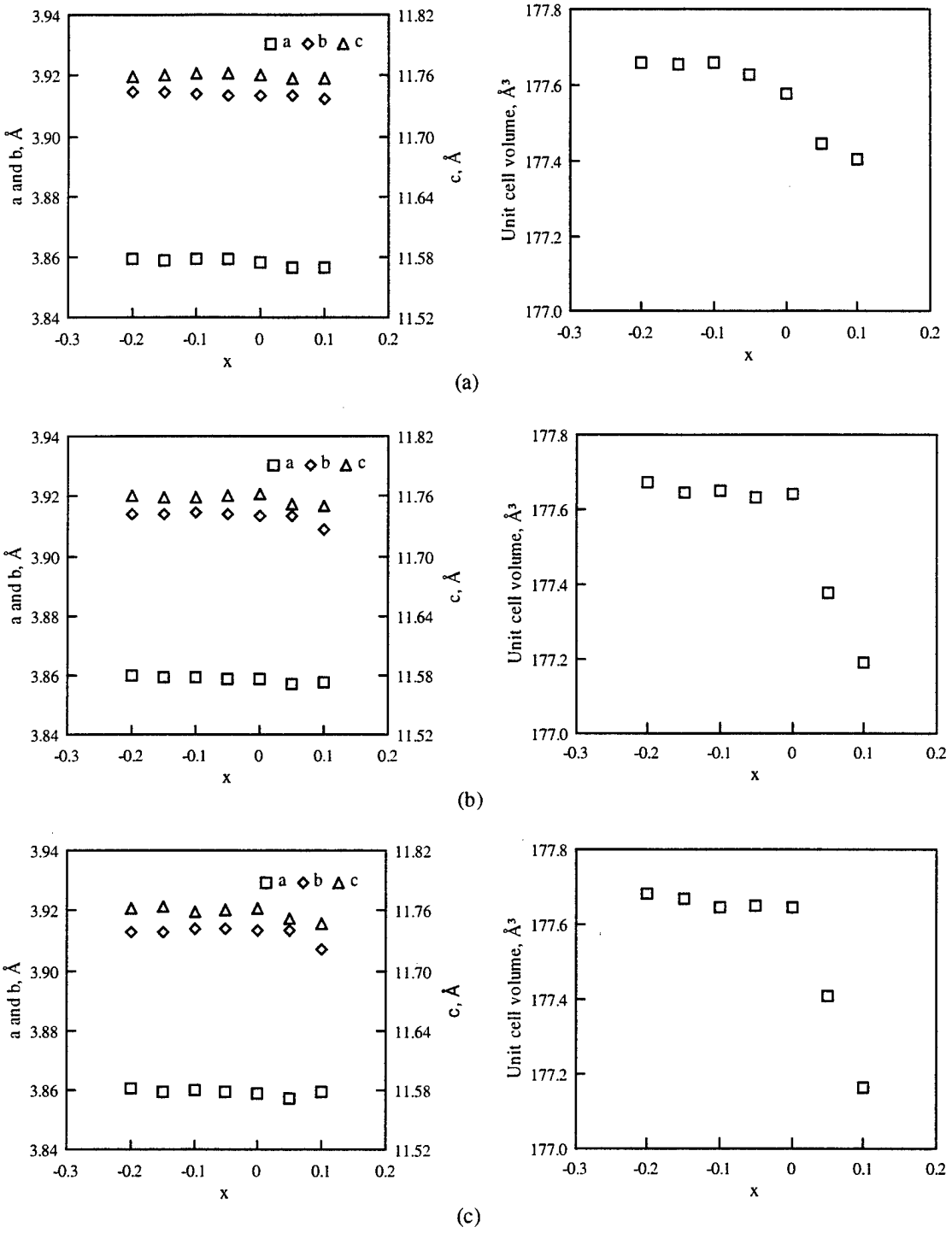

Figure 29 Lattice parameters and unit cell volume of Nd123ss treated in 0.001 bar Po_2 at (a) 990°C, (b) 915°C and (c) 900°C.[87]

show the changes in lattice parameters and unit cell volume with composition at 900°, the eutectic temperatures and 20°C below the peritectic temperatures of Nd123 in 1 bar, 0.2 bar, 0.01 bar and 0.001 bar Po_2. The measurement errors are about the size of the symbols in the figures. Some slight fluctuations of the data are caused by the variation of oxygen content due to differences in particle size and density, especially for the batches annealed at 350°C. It can be seen that the lattice parameters b and c are more affected by the composition than the lattice parameter a. Obviously, the unit cell volume is more sensitive in determining the lower solubility limits. For samples with x less than the solubility limit, no change in the unit cell volume is expected. As x enters the region of solid solution, a deviation in the unit cell volume will occur. In combination with the phase information in Table 8 and the DTA data in Figure 24, we can determine the lower solubility limits of Nd123ss in the different Po_2's, as shown in Table 9.

Table 9 Lower Solubility limit for $Nd_{1+x}Ba_{2-x}Cu_3O_{7-y}$.[87]

Po_2, bar	Temperature, °C	Lower solubility limit x
1	1070	0
	1030	0
	900	0.05
0.2	1050	0
	998	0
	900	0.05
0.01	1010	0
	937	0
	900	0
0.001	990	0*
	915	0
	900	0

* Very narrow solid solution range near x=0, which may extend to Cu-rich region

In 1 bar and 0.2 bar Po_2, we see a decrease in solubility at lower temperatures. This confirms the trend observed by Osamura and Zhang in air.[33] However, our data show that the solid solution never extends below x = 0. That means there is negligible net substitution of Ba^{2+} for Nd^{3+}. The lower solubility limit of Nd123ss in air is perhaps overestimated in the study by Osamura and Zhang,[33] which reaches x = ~-0.1 at the eutectic temperature. In 0.01 bar and 0.001 bar Po_2, although the XRD peaks of $BaCuO_2$ may not be detected (Table 8), the unit cell volume data shows that the lower solubility limits remain at the stoichiometric composition of x = 0. Goodilin et al.[92] also reported a solid solution range to x = -0.1 at 850°C in nitrogen (The actual Po_2 is not well defined). In our laboratory commercial nitrogen has an Po_2 of about $3x10^{-5}$ bar. Our present study does not cover such a low Po_2. The difficulty with detection of the minor second phase may be due to the fine size formed during quenching or that it may simply exist as an amorphous phase.

The solid solution range of the batch of samples treated at 990°C in 0.001 bar Po_2 deserves extra discussion. From the unit cell volume data in Figure 29.a, there is a small solid solution range from $x \approx -0.05$ to $x \approx 0.05$ as the unit cell volume continues to decrease with x. But the XRD patterns clearly indicate second phases for x = -0.05 and x = 0.05, as shown in Figure 30. One of the second phases is Nd422. The other unidentified peaks are presumably from phases formed from the liquid on quenching. The peak positions are close to those of $Ba_2Cu_3O_5$ but the intensities do not agree well with the values reported in the JCPDS database. This is perhaps caused by the formation of a solid solution of this phase and/or the existence of other minor phases. The existence

of second phases implies that the solid solution is limited to a very narrow range of -0.05 < x < 0.05 along the $Nd_{1+x}Ba_{2-x}Cu_3O_7$ composition line, otherwise no second phase will appear in the solid solution range between Nd and Ba. The decrease of unit cell volume may be caused by a slight change of oxygen content or it may indicate that the solid solution extends into the Cu-rich range as Cu^{2+} is smaller than Nd^{3+} and Ba^{2+}. In

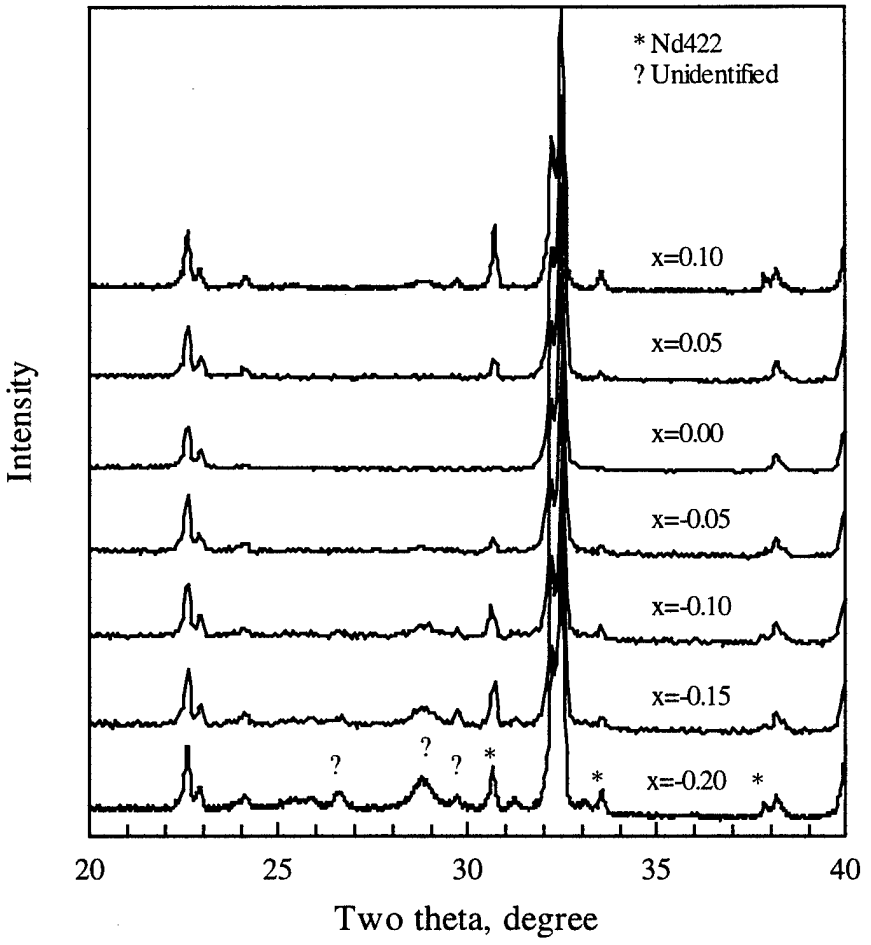

Figure 30 XRD of Nd123ss treated at 990°C in 0.001 bar Po_2.[87]

consideration of the size difference, an increase in the Cu amount from 3 to 3.01-3.02 in $Nd_{1+x}Ba_{2-x}Cu_3O_7$ is perhaps enough to cause such a change in the unit cell volume, which is difficult to measure experimentally in a phase mixture. The single crystal grown in 0.01 bar Po_2 by Nakamura et al.[93] has a composition of Nd:Ba:Cu = 1.01:1.97:3.00, which is slightly Cu-rich. However, definite conclusion cannot be drawn due to the limit of the experimental accuracy.

The change in lower solubility limits with Po_2 can be used to produce flux pinning centers. As Nd123 processed in low Po_2 is annealed in oxygen, second phases will be precipitated out. We can sketch a phase diagram of Nd-Ba-Cu-O in 1 bar Po_2 (Figure 31). At high temperature, the equilibrium second phase $BaCuO_2$ is formed. According to the thermodynamic calculation of Voronin and Degterov,[94] $BaCuO_2$ will decompose into $Ba_2CuO_{3.3}$ and $Ba_2Cu_3O_{5+y}$ at low temperature:

$$8\ BaCuO_2 + (0.3+y)\ O_2 = 2\ Ba_2CuO_{3.3} + 2\ Ba_2Cu_3O_{5+y}$$

$$\log [\ Po_2\ (atm)] = 8.1400 - 7172.1/T\ (K)$$

This gives us the decomposition temperature of 608°C in 1 bar Po_2. To verify this reaction, a sample of $BaCuO_2$ and a sample of Nd123ss (x = -0.1) with $BaCuO_2$ as a minor phase were annealed in 1 bar Po_2 with continuous cooling from 600°C to 400°C for seven days. The $BaCuO_2$ sample showed partial decomposition according to the above reaction but no other second phases were detected in the Nd123ss sample. This indicates that the reaction is kinetically sluggish. As a result, the equilibrium second phases may not form during the low temperature oxygen annealing of Nd123 and it is likely that some metastable transition phase may precipitate out.

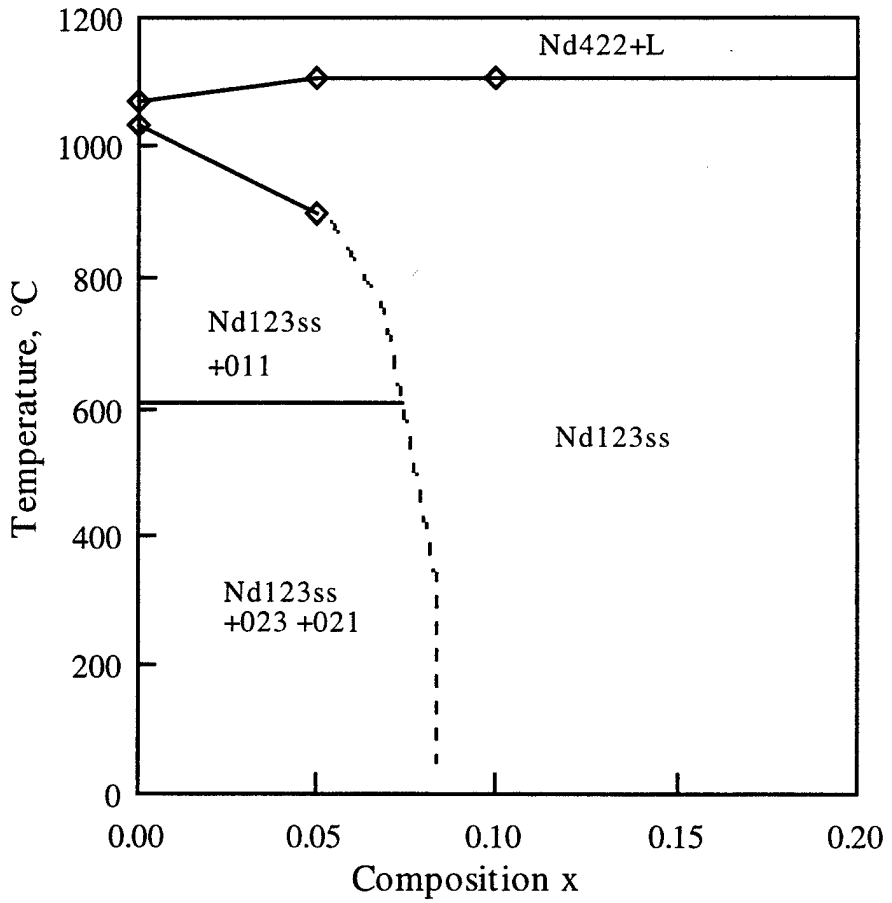

Figure 31 Phase diagram of Nd123 in 1 bar Po_2.[87]

B. Precipitation in Nd123ss

To verify the precipitation process, melt-texture growth was conducted in 500 ppm oxygen. Typical fracture surfaces of the as-grown samples are shown in Figure 32. The broad surface is the a-b plane of the sample. It can be seen that the grains are well aligned in the c-axis.

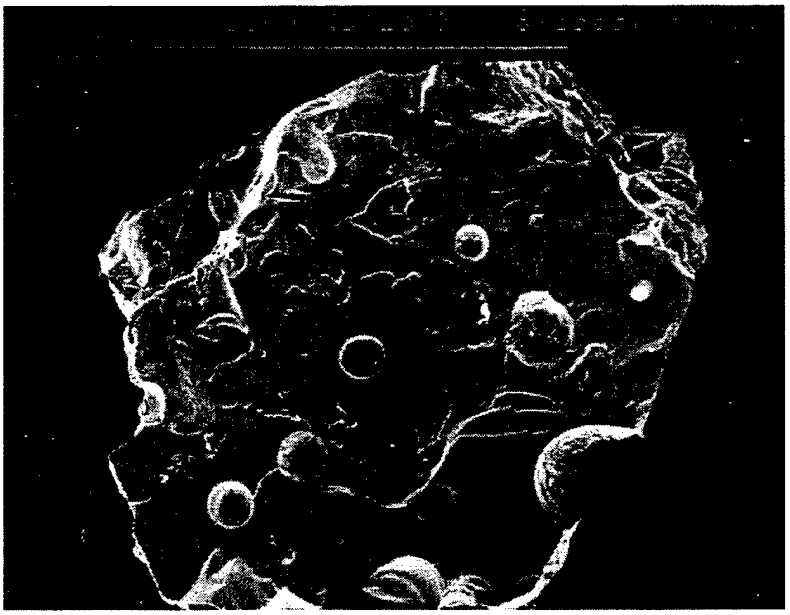

(a)

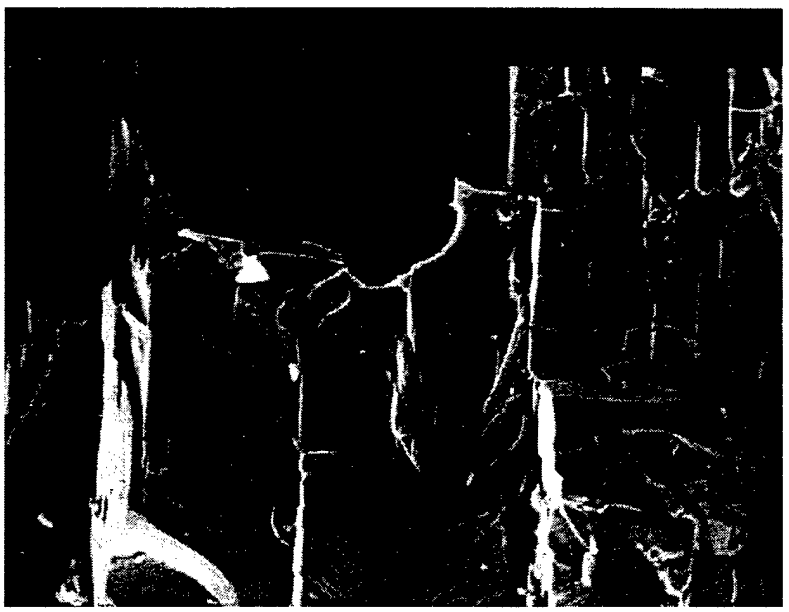

(b)

Figure 32 SEM of a typical melt-textured sample shows (a) the broad surface of a-b plane and (b) the alignment viewed from the edge. Big Nd422 particles are also shown.

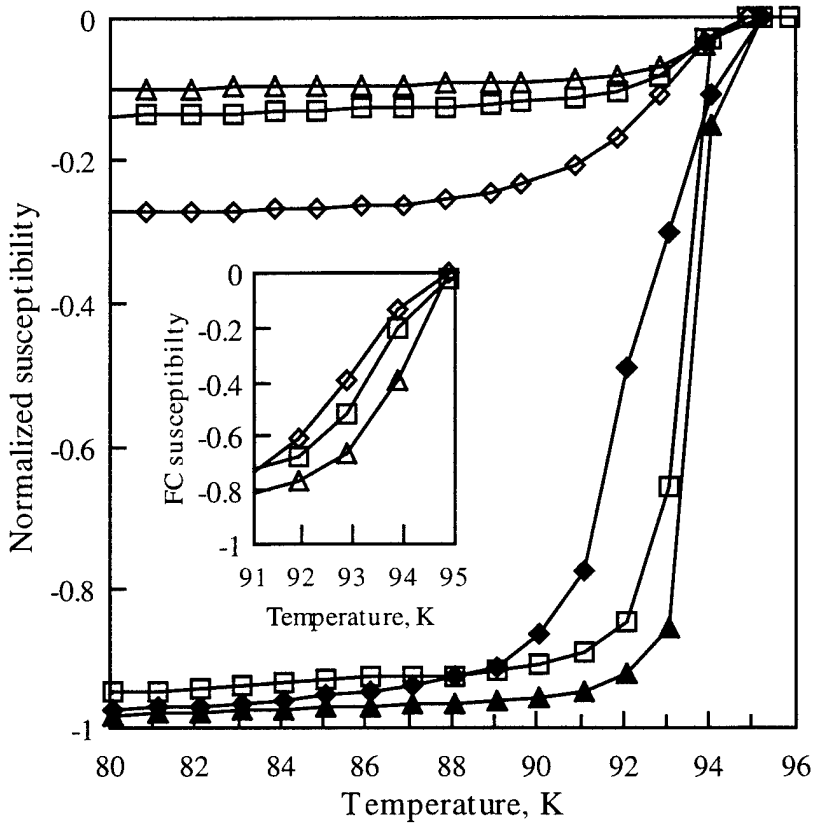

Figure 33 DC magnetization normalized to the zero field cooled (ZFC) values at 10K. [95] The inset is the normalized field cooled (FC) data. The field of 10 Oe is applied parallel to the c-axis. Close symbols are for ZFC data and open symbols are for FC data. The annealing temperatures are 350°C (square), 500°C (triangle) and 900°C (diamond) respectively.

DC magnetization of the oxygen annealed samples shows that all the samples have sharp superconducting transitions with the onset T_c of about 95 K (Figure 33). T_c (midpoint) changes slightly with the oxygen annealing treatments. There is a slight increase in T_c with the increase of the annealing temperature from 350°C to 500°C, but T_c is lowered by about 1 K when the annealing temperature is increased to 900°C. With the same final oxygen annealing at 350°C for 96 hr, the change in T_c is not caused by the

oxygen contents of the samples, rather it is due to the gradual shift of the matrix composition to larger x in $Nd_{1+x}Ba_{2-x}Cu_3O_{7-\delta}$ as a result of narrowing of the solid solution range during the annealing process. The matrix composition should be in the range of x = 0.05~0.08 as we compare the effect of composition on T_c in the literature.[27]

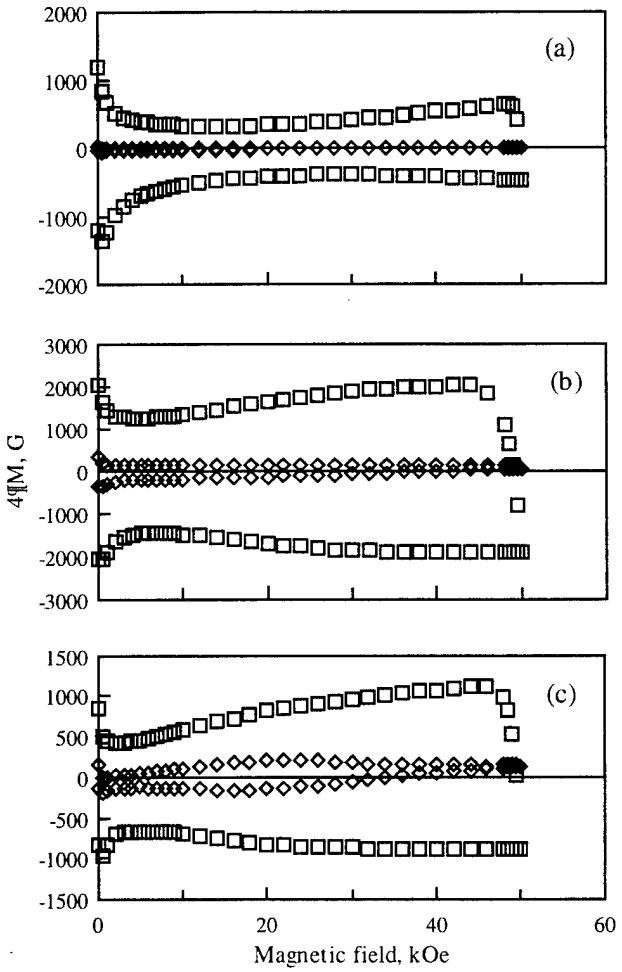

Figure 34 Hysteresis loops with H // c at 50 K (square) and 77 K (diamond) of samples oxygen annealed at (a) 350°C for 96 hr, (b) 500°C for 96 hr plus 350°C for 96 hr, and (c) 900°C for 48 hr plus 350°C for 96 hr.[95] The J_c's are estimated by Bean's model to be 70, 120, 70 kA/cm^2 at 50 K and 44 kOe respectively, and 0.5, 9.2, 12.5 kA/cm^2 at 77 K and 20 kOe respectively.

The peak effect in the hysteresis loops for the applied field parallel to the c axis is clearly seen at 50 K for all the samples with the maximum beyond the measurement range of 50 kOe (Figure 34). At 77 K the peak effect is not seen for the sample annealed at 350°C. While there is room for optimizing the process to improve flux pinning, the purpose is to clarify the flux pinning mechanism.

TEM was performed on a sample annealed at 500°C for 96 hr and 350°C for 96 hr. The sample was crushed in a mortar into small crystals suspended in ethanol. These small crystals were floated onto a gold mesh for TEM observation in a Philips C30 operated at 300 KeV. Figure 35 shows the existence of stacking faults and a high density of dislocations in addition to the twin structure. A lattice image taken with the beam parallel to [100] or [010] direction shows extra layers of atoms (stacking faults) with a spacing of 3~8c (c = 1.176 nm) between them (Figure 36). The size of the extra layer is about one third of c. The defect is coherent with the matrix. It is also observed that the presence of this defect causes a slight deformation of the planes on either side of the defect, suggesting some mismatch strain as indicated by the streaking along c* in the selected area diffraction pattern. Based upon mass balance and structure, this defect is most consistent with an extra perovskite layer of $BaCuO_2$ as shown in Figure 37. Computer simulation of the image matches well with this model. With an overall stoichiometric composition, the precipitation of $BaCuO_2$ with an average spacing of 5c will give a matrix composition of $x = 0.06$ which matches well with the lower solubility of $x \approx 0.05$ in oxygen. Similar extra perovskite layer has also been observed in $YBa_2Cu_3O_{7-\delta}$ system, which is explained as a response to the stoichiometry constraint of

the line compound.[96] In the Nd123ss system, the planar defect is formed as an intermediate structure in the precipitation process due to the change of the lower solubility limit. This coherent structure has a very low interfacial energy, and thus significantly decreases the nucleation barrier. Therefore, it forms as the first precipitate. Given enough time, the equilibrium precipitates will eventually form.

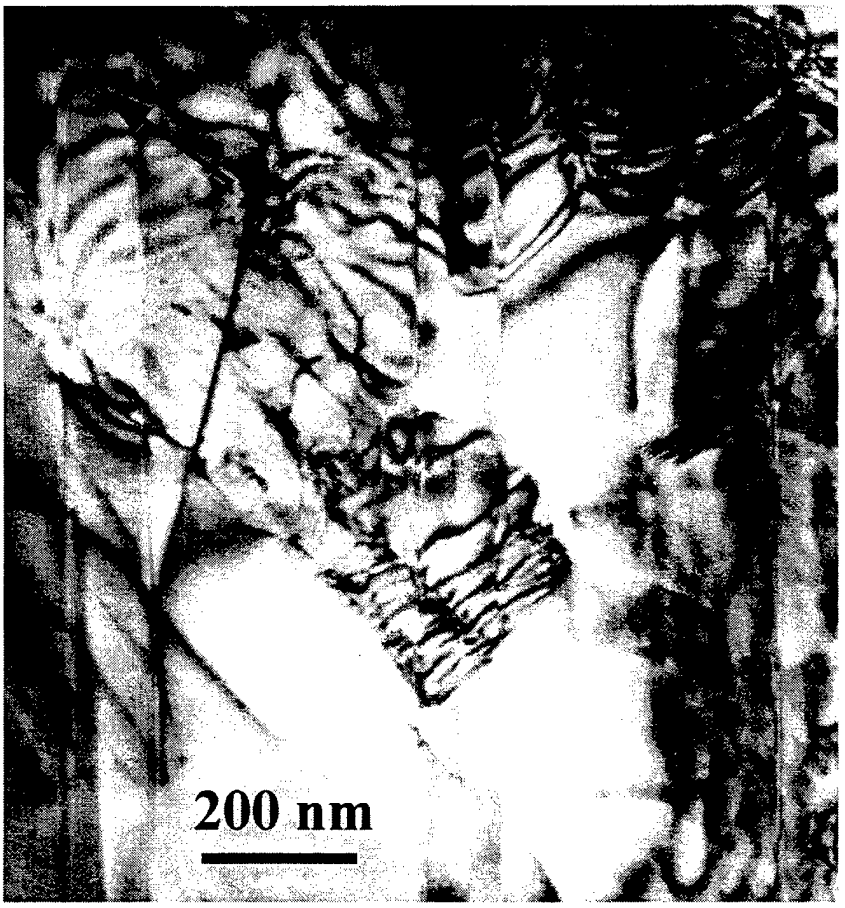

Figure 35 TEM image shows twin structure, dislocations, and stacking faults.[95] The stacking faults (center) are out of contrast but the associated dislocations are in contrast. The arrow indicates $\mathbf{g}_{200}$.

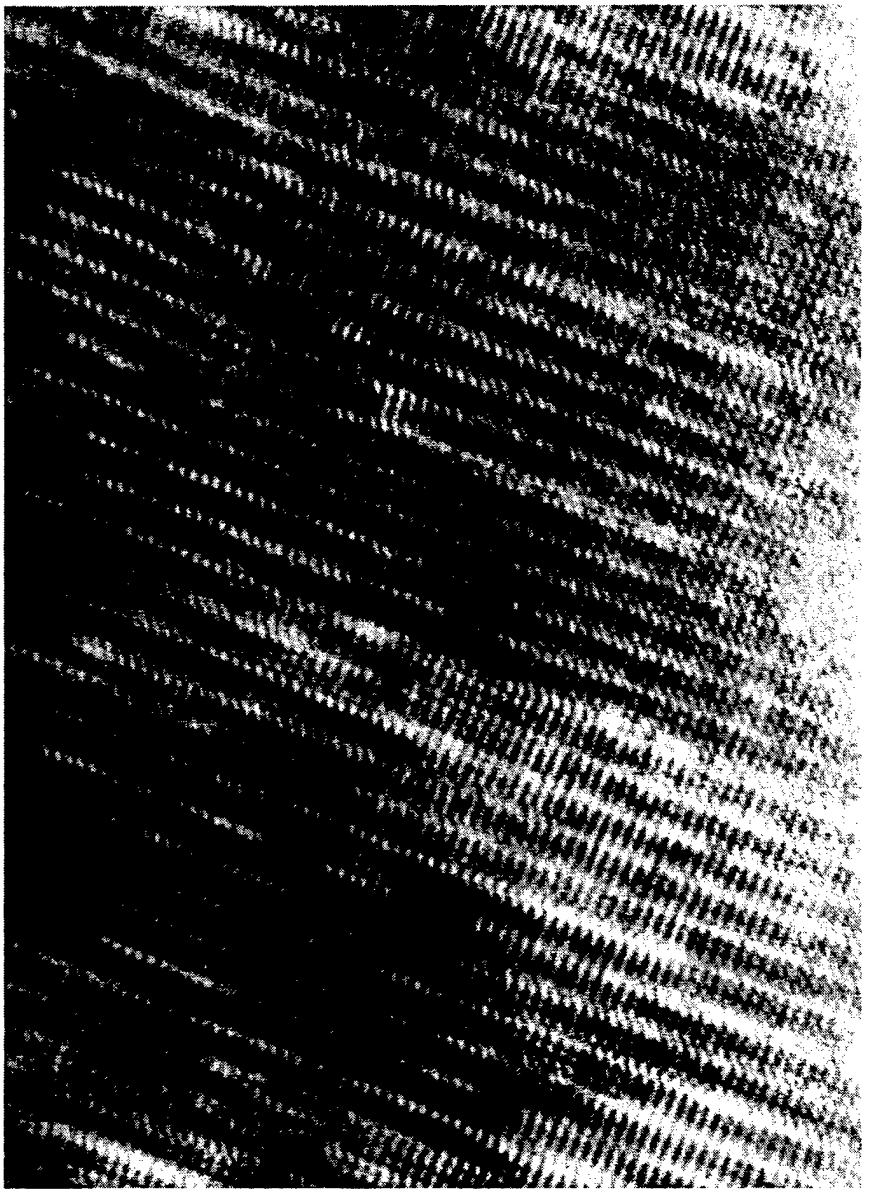

Figure 36 Lattice image of the defect structure. Extra layers of atoms appear with a spacing of 3-8c.

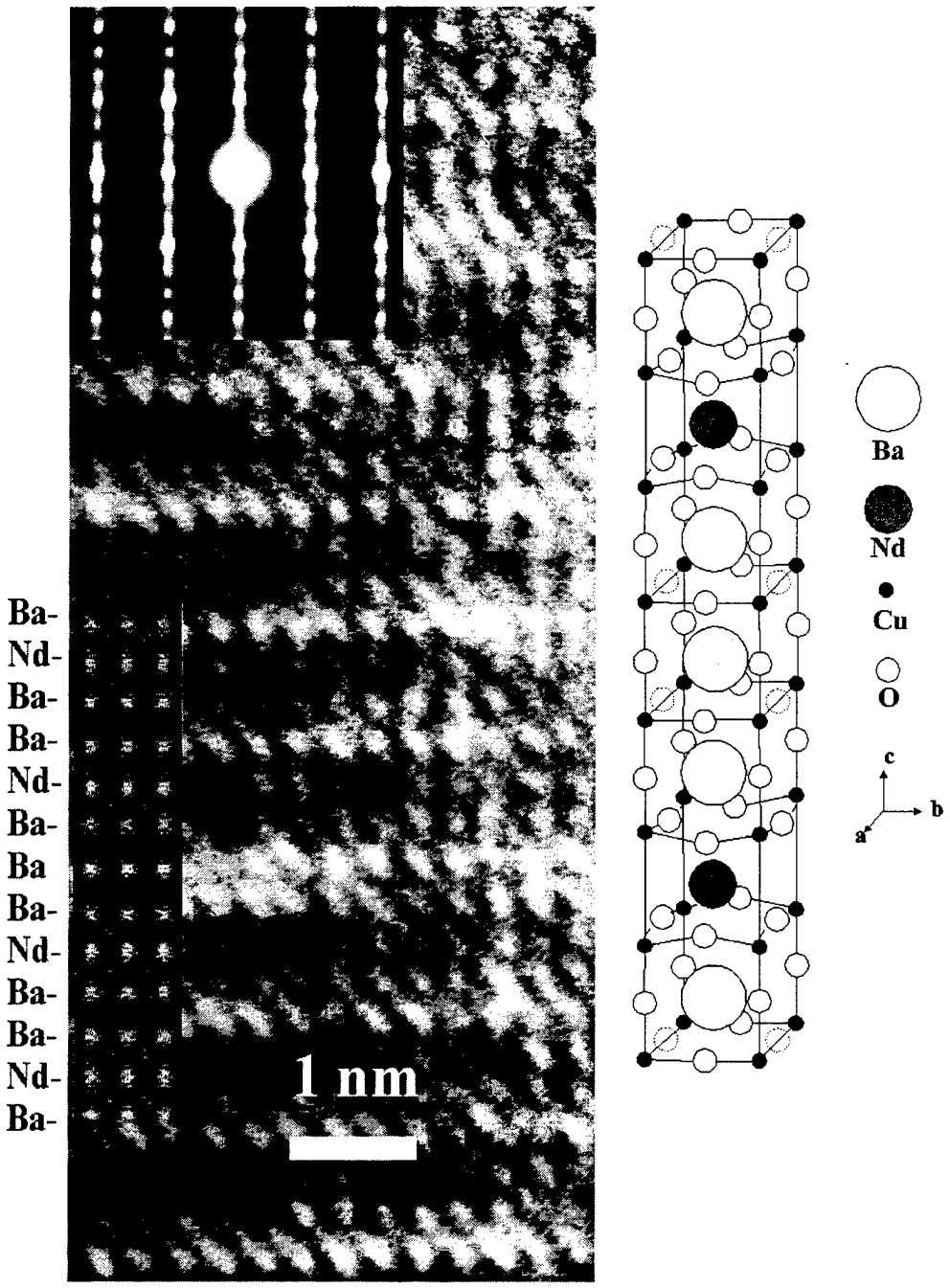

Figure 37 Lattice image of the defect structure.[95] The inset in the TEM image is the computer simulation of the proposed structure model, in which an extra layer of $BaCuO_2$ is inserted between Nd123ss unit cells. The selected area diffraction pattern shows streaking in c* due to lattice distortion consistent with the model proposed.

We believe that the planar defect and a high density of dislocations caused by precipitation are responsible for the enhanced flux pinning. The amount of precipitates is determined by the compositional difference of the as-grown sample and the lower solubility limit at the oxygen annealing temperature as well as kinetic factors. During melt-texture growth, the composition of the solid Nd123ss phase will follow the solidus line. For low Po_2 the slope of the solidus with respect to temperature is relatively steep, so the solid is very close to the stoichiometric composition independent of the starting composition of the sample. Since the lower solubility limit for Nd123ss in oxygen is around $x = 0.05$, precipitation will occur for $x < 0.05$ and no precipitation will occur for Nd123ss with an actual composition of larger x. This prediction is in agreement with recent J_c results.[97,98] The peak effect is observed for Nd123ss with an actual composition of $x \approx 0$[97] but not for Nd123ss with $x = 0.06$ [98] or 0.08-0.11.[97] While high T_c and enhanced pinning have been observed for starting compositions of $x = 0.15$[99] and $x = 0.2$,[100] the processing conditions were such that the actual composition of the superconducting phase should be near stoichiometric Nd123. In fact, the overall composition for the $x = 0.2$ sample processed in this fashion was measured at $x = 0.04$ (or Ba/Nd ratio of 1.88).[100]

The presence of the peak effect of Nd123ss prepared in low Po_2 is clear evidence of enhanced pinning but does not provide much insight into the origin of the pinning.[9,37,88,97,99-103] Such a peak effect has been produced by vortex and defect interaction in Y123 with columnar defects.[104] From the pinning point of view, the assumption that as-grown Nd123ss is decomposed into a high T_c Nd123 phase and a Nd123ss ($x > 0$)

with a lower T_c, perhaps about 70 K[101] or a nonsuperconducting Nd123ss (x = 0.8),[103] is reasonable. This assumption attributes the peak effect to field induced quenching of the low T_c phase at high temperature and high field.[37,88,97,99-103] However, there are a number of problems with this idea. The phase separation is attributed to a spinodal decomposition of the Nd123ss. In the case where the two end points are x = 0 and x = 0.12, a sample with $x \approx 0.06$ should phase separate into approximately equal fractions of material with Tc > 90 K and Tc ~70 K. In fact, for x = 0.05 we observe a sharp transition with an inductive onset of 95 K and no indication of a second phase. For the case where the end points are x = 0 and $x \approx 0.8$,[103] a sample with x = 0.3-0.4 should be expected to have a significant superconducting fraction which is not the case. In addition, strong flux pinning should be seen in samples with an overall composition around x = 0.1. So far, well characterized samples with overall composition of x = 0.1 give neither high T_c (~95K)[91] nor peak effect.[97] Therefore, the phase separation assumption contradicts the continuous solid solution range observed in this system. It should be pointed out that composition variation during the solidification of a solid solution is expected. This may cause misleading interpretation as flux pinning centers. The scanning tunneling microscopy and spectroscopy results of Ting et al.[102] are not rigorously quantitative so that the second phase can also be interpreted as Ba-rich precipitates.

Melt-texture growth was performed in the same way for a starting composition of Nd123ss (x = -0.1) to see whether the lower solubility limit is extended in 500 ppm oxygen. XRD results of the as-grown sample show Nd123 phase and minor Nd422 phase which are similar to the XRD results for Nd123 samples. Tc and hysteresis

measurements also give similar results. Figure 38 shows the hysteresis loops for a Nd123ss sample with a starting composition of x = -0.1 annealed at 900°C for 48 hr and 350°C for 96 hr. We can see the loop is still open even at 85 K. For samples with a starting composition of $x < 0$, the composition of the formed phase will change along the left side of the composition with the maximum melting temperature (refer to Figure 25). This will facilitate the formation of Nd123ss close to the stoichiometric composition. On the other hand, the composition with the maximum melting temperature shifts to lower x value with decreasing Po_2. At a sufficiently low Po_2, it may reach a value of negative x. The solubility limit at $Po_2 < 0.001$ bar deserves further study.

At present, systematic study of the effects of precipitation has not been conducted. At temperature around 500°C, the coherent intermediate perovskite structure with a composition of $BaCuO_2$ is observed during the precipitation process along with a high density of dislocations. At high temperature of 900°C, it is believed that the equilibrium $BaCuO_2$ phase is formed. Nakamura et al.[93] performed oxygen annealing of Nd123 at 340°C, 400°C, 500°C and 600°C for 200 hr. It is found that annealing at low temperatures of 340°C and 400°C and the intermediate temperature of 600°C does not show enhanced flux pinning. Therefore, we can sketch the precipitation processes as shown in Figure 39. The actual temperature and time range will depend on the composition of the Nd123ss obtained in the melt-texture process. The flux pinning ability is related to the amount, size, shape, and distribution of the precipitates, which are controlled by the melt-texture growth process and the precipitation process.

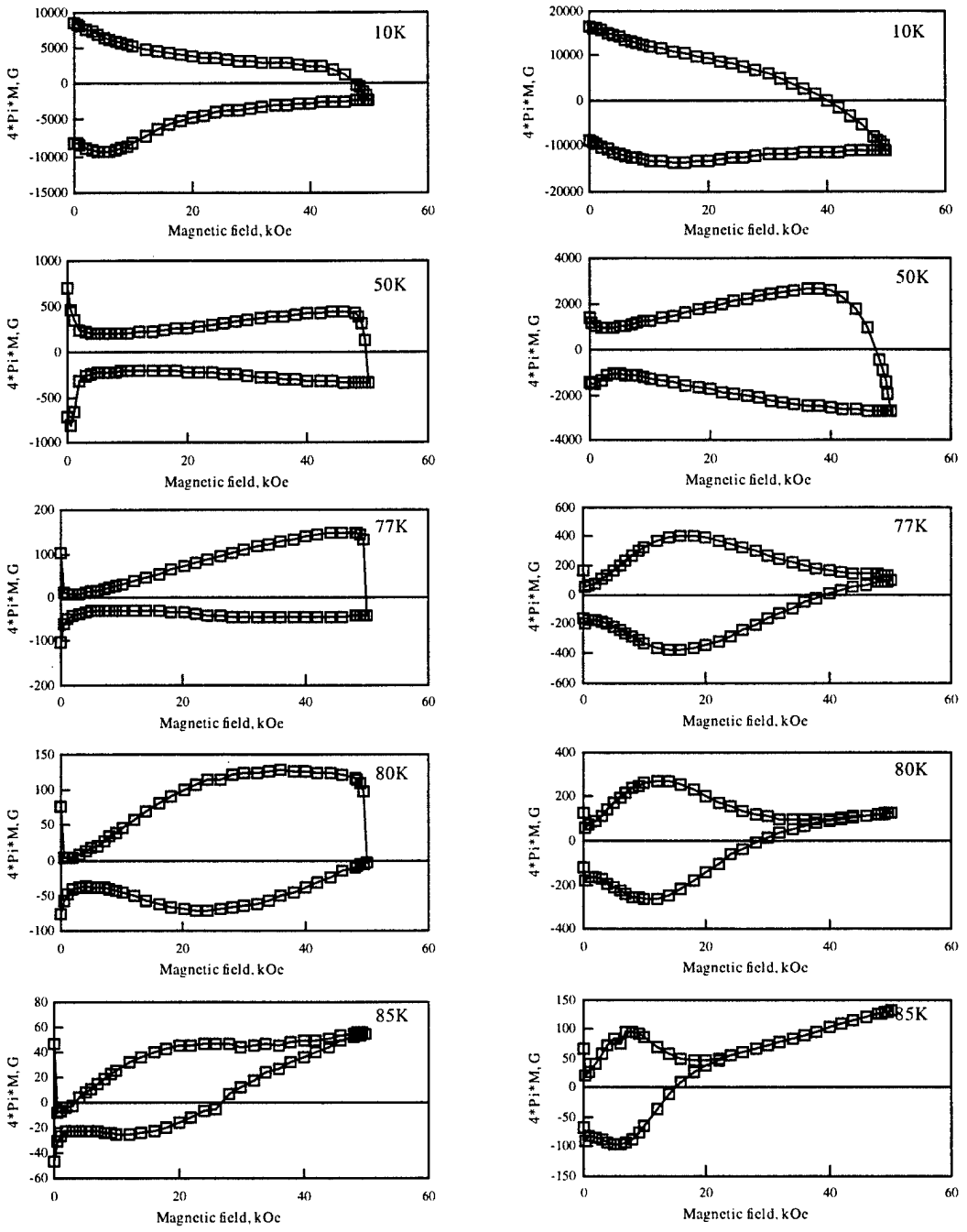

Figure 38 Hysteresis loops for Nd123ss with a starting composition of x = -0.1 annealed at 900°C for 48 hr and 350°C for 96 hr with (a) H ⊥ c-axis and (b) H // c-axis. Sample size: 0.60x0.60x0.30 mm^3.

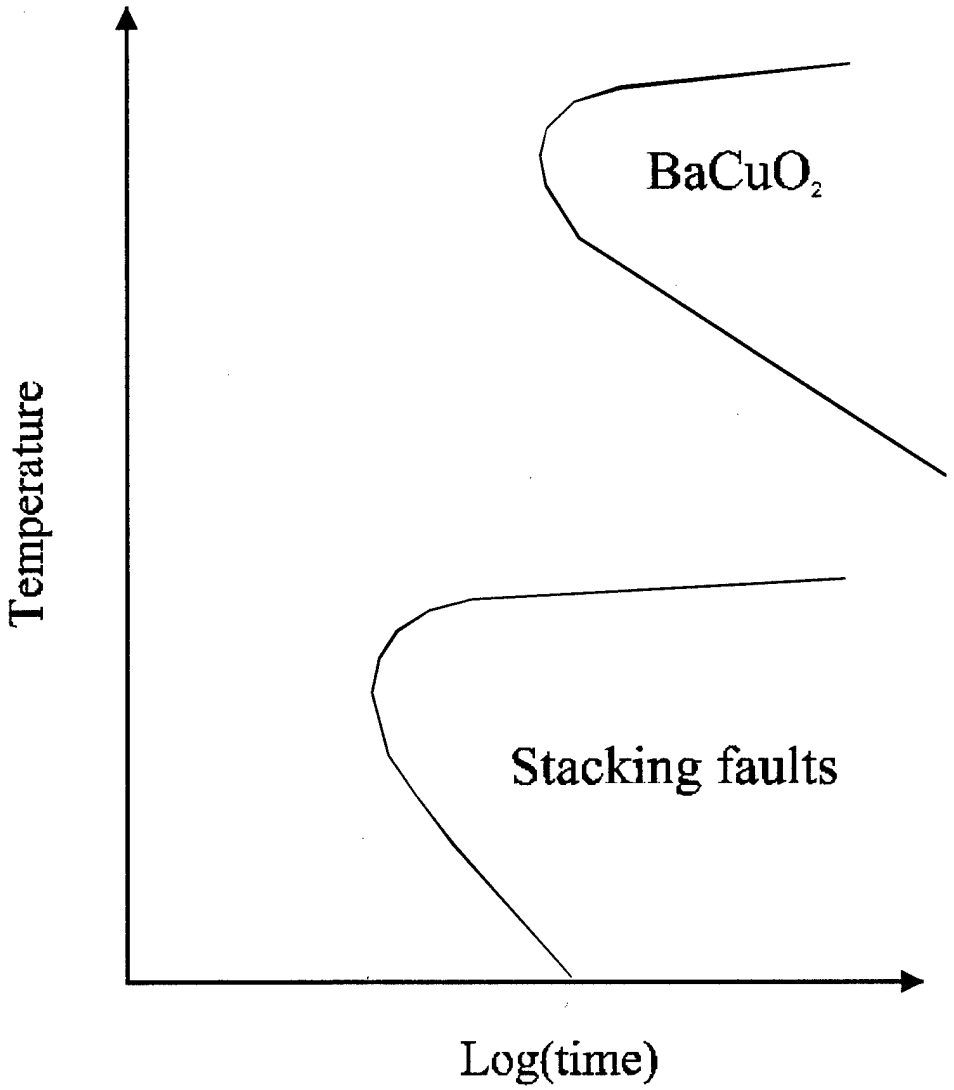

Figure 39 Schematic diagram illustrating the precipitation processes in Nd123ss.

CHAPTER V CONCLUSIONS

1. Summary

Precipitation processes were developed to introduce second phases as flux pinning centers in Gd-Ba-Cu-O and Nd-Ba-Cu-O superconductors. In Gd-Ba-Cu-O, precipitation is caused by the decrease of the upper solubility limit of Gd123ss in low Po_2. In Nd-Ba-Cu-O it is caused by the decrease of the lower solubility limit of Nd123ss in oxygen.

Processing of supersaturated $Gd_{1.2}Ba_{1.8}Cu_3O_7$ in low Po_2 can produce dispersed second phases. It is found that Gd211 is formed as a separate phase while extensive stacking fault is formed instead of a separate CuO phase. It is believed that the stacking fault is of the 124 type with a CuO layer between the 123 unit cells. As a result of the precipitation reaction, T_c can be increased to that of Gd123. The size and distribution of the second phases need to be optimized for better enhancement of J_c. The process can be adapted to existing processing methods to obtain strong flux pinning while avoiding grain boundary weak links.

The lower solubility limits of Nd123ss in 1 bar, 0.2 bar, 0.01 bar and 0.001 bar Po_2 were studied by DTA and XRD. The DTA results reveal the relative stability of Nd123ss in different Po_2's. In 1 bar Po_2, Nd123ss with $x = 0.1$ is the most stable phase. In lower Po_2's, the most stable composition shifts towards the stoichiometric composition. The relative stability changes faster with decreasing Po_2. Therefore, processing in oxygen and air tends to produce broad superconducting transitions but sharp transitions can be achieved in 0.01 bar and 0.001 bar Po_2. While the lower

solubility limits in 0.01 bar and 0.001 bar Po_2 remain at x = 0.00, the solubility limits in 1 bar and 0.2 bar Po_2 show a narrowing with decreasing temperature. Because of the narrowing of the solubility range in 1 bar Po_2, oxygen annealing of Nd123 initially processed in low Po_2 will result in precipitation of second phases. The equilibrium second phase is $BaCuO_2$ for temperature above 608°C, and at lower temperatures the equilibrium second phases are $Ba_2CuO_{3.3}$ and $Ba_2Cu_3O_{5+y}$. However, annealing at low temperatures produces a fine metastable transition phase.

Melt-texture growth was conducted for Nd123 in 500 ppm oxygen at ambient pressure. A coherent intermediate perovskite structure with a composition of $BaCuO_2$ (stacking fault) is observed along with a high density of dislocations during the oxygen annealing at 500°C for 96 hr. It is believed that oxygen annealing at 900°C produces the equilibrium $BaCuO_2$ phase. These precipitates are responsible for the strong flux pinning in Nd123 melt-textured in low Po_2.

2. Recommendations for future research

This work opens a new direction to introduce flux pinning centers in R123 superconductors. More work is needed to fully understand the precipitation processes and to optimize the processing conditions for better J_c.

Thermodynamic data of the solid solutions and related phases in different Po_2 is very useful information. On the one hand, the solubility limits at low temperatures cannot be determined by the method used in this research but they can be calculated from thermodynamic data. On the other hand, the driving force for precipitation can be

estimated from such data.

In Gd123ss, the nucleation density of Gd211 phase seems to be very low. It is necessary to study the nucleation process in order to find a way to increase the nucleation rate of Gd211 and thus increase the precipitation kinetics. If dislocation is the heterogeneous nucleation center, perhaps pre-deformation will increase the nucleation rate and therefore further reduce the size of Gd211 phase.

In Nd123ss, it is believed that vacancies may play an important role in the precipitation process. Therefore, the melt-texture temperature and quenching rate may have an effect on the precipitation process. The composition of the supersaturated solid solution, the annealing temperature and annealing time will affect the amount, shape, size, and distribution of the precipitates, which determine the effectiveness of flux pinning of the precipitates. More work is needed to determine the optimal processing conditions: temperature, Po_2, cooling rate, oxygen annealing temperature and time.

Both processes have the potential to be incorporated into a manufacturing process to produce superconductors with improved properties. Alternative processing method other than melt-texture growth method may also be developed.

REFERENCES

[1] M. Ueyama, T. Hikata, T. Kato, and K. Sato, Jpn J. Appl. Phys., 30, 1384 (1991)

[2] P. Haldar, J. G. Hoelm, Jr. U. Balachandran, and L. R. Motowidlo, Proc. Symp. on "Processing of Long Lengths of superconductors", 1993 TMS-AIME Fall Meeting, Pittsburgh, Oct. 17-21, 1993

[3] S. Jin, R. B. van Dover, T. H. Tiefel, J. E. Graebner, and N. D. Spencer, Appl. Phys. Lett, 58, 868 (1991)

[4] S. Jin and C. W. Chu, in Processing and Properties of High T_c Superconductors, Vol.1, ed. S. Jin, World Scientific, Singapore, p87 (1993)

[5] S. Jin, T. H. Tiefel, R. C. Sherwood, M. E. Davis, R. B. van Dover, G. W. Kammlott, R. A. Fastnacht, and H. D. Keith, Appl. Phys. Lett. 52, 2074 (1988)

[6] K. Salama, V.Selvamanickam, L. Gao, and K. Sun, Appl. Phys. Lett. 54, 2352 (1989)

[7] M. Murakami, M. Morita, K Doi, and K. Miyamoto, Jpn. J. Appl. Phys. 28, 1189 (1989)

[8] P. J. McGinn, W. Chen, N. Zhu, U. Balachandran, and M. T. Lanagan, Physica C165, 480 (1989)

[9] S. I. Yoo, N. Sakai, H. Takaichi, T. Higuchi, and M. Murakami, Appl. Phys. Lett, 65, 633 (1994)

[10] M. J. Cima, M.C. Flemings, A.M. Figueredo, M. Nakade, H. Ishii, H.D. Brody, and J. S. Haggerty, J. Appl. Phys. 72, 179 (1992)

[11] T. Izumi, Y. Nakamura, and Y. Shiohara, J. Cryst. Growth 128, 757 (1993)

[12] M. Murakami,in Processing and Properties of High T_c Superconductors, Vol. 1, ed. S. Jin, World Scientific, Singapore, p217 (1993)

[13] M. Morita, S. Takebayashi, M. Tanaka, K. Kimura, K. Miyamoto, and K. Sawano, Adv. in Supercon. 3, 733 (1991)

[14] C. Varanasi, P. J. McGinn, Physica C 207, 79 (1993)

[15] C. Varanasi, S. Sengupta, P. J. McGinn, and D. Shi, Appl. Supercond. 1, 71 (1993)

[16] S. Jin, T.H. Tiefel, S. Nakahara, J.E. Graebner, H.M. O'Bryan, R. A. Fastnacht, and G.W. Kammlott, Appl. Phys. Lett. 56, 1287 (1990)

[17] M. A. Kirk and H. W. Weber, in Studies of High Temp. Superc., A. Narlikar ed. Vol 10, Nova, p243-304 (1992)

[18] P. C. Johnston, A. J. Jacobson, J. M. Newsam, J. T. Lewandowski, D. P. Groshorn, D. Xie, W. D. Yelon, Chemistry of High T_c Superconducting Oxides, (ACS Sypm. Ser. 351), Washington, American Chem. Soc., p136 (1987)

[19] P. Karen, O. Braaten, and A. Kjekshus, Acta Chemica Scandinavica, 52, 805 (1992)

[20] R. Beyers, B. T. Ahn, G. Gorman, and V. Y. Lee, Nature, 340, 619 (1989)

[21] L. E. Levine and M. Daumling, Phys. Review B45, 8146 (1992)

[22] R. J. Cava, P.B. van Dover, B. Batlogg, and E. A. Rietman, Phys. Review Lett., 58, 408 (1987)

[23] B. W. Veel, A. P. Paulikas, H. You, H. Shi, Y. Fang, and J. W. Downevy, Phys. Review B42, 6305 (1990)

[24] Beyers, T. M. shaw, Solid State Phys. 42, 135 (1989)

[25] M. Guillaume, P. Allenspach, J. Mesot, B. Roessli, U. Staub, P. Fischer, A. Furrer, Z. Phys. B90, 13 (1993)

[26] K. Zhang, B. Dabrowski, C. U. Segre, D. G. Hinks, I. K. Schuller, J. D. Jorgenson, and M. Slaski, J. Phys. C20 L935 (1987)

[27] M.J. Kramer, S. I. Yoo, R. W. McCallum, W. B. Yelon, H. Xie, and P. Allenspach, Physica C 219, 145 (1994)

[28] S.I. Yoo and R. W. McCallum, Physica C 210, 147 (1993)

[29] R.D. Shannon, Acta Cryst. A32, 751 (1976)

[30] W. Wong-Ng, B. Paretzkin, and E. R. Fuller, Jr., Advances in X-ray Analysis, 33, 453 (1990)

[31] F. Abbattista, M. Vallino, and D. Mazza, Mater. Chem. Phys., 24, 363 (1990)

[32] R. Beyers and T. M. Shaw, Solid State Phys. 42, 135 (1989)

[33] K. Osamura and W. Zhang, Z Metallkd., 84, 523, (1993)

[34] R. W. McCallum. M. J. Kramer, K. W. Dennis, M. Park, H. Wu, and R. Hofer, J. Electronic Mater., 24, 1931 (1995)

[35] T. Aselage and K. keefer, J. Mater. Res., 3, 1279 (1988)

[36] J. E. Ullman, R. W. McCallum, and J. D. Verhoeven, J. Mater. Res., 4, 752 (1989)

[37] M. Murakami, N.Sakai, T.Higuchi, and S.I. Yoo, Superconductor Sci. Tech., 9, 1015 (1996)

[38] T. B. Lindemer, J. F. Hunley, J. E. Gates, A. L. Sutton, J. Brynestad, C. R. hubbard, and P.K. Gallagher, J. American Ceramic Soc., 72, 1775 (1989)

[39] R. Beyers and B. T. Ahn, Annual Review of Mater. Sci., 21 335 (1991)

[40] R. Bormann and J. Nolting, Appl. Phys. Lett, 54, 2148 (1989)

[41] J. Kim and D. R Gaskel, J. American Ceramic Soc., 77, 753 (1994)

[42] G. Ceder, M. Asta, D. de Fontaine, Physica C177, 106 (1991)

[43] M.J. Kramer, H. Wu, K. W. Dennis, and R.W. McCallum, J. Electronic Mater., in press

[44] H. Wu, M.J. Kramer, K. W. Dennis, and R.W. McCallum, IEEE Trans. Appl. Superconductivity, in press.

[45] J.L. Routbort and S.J. Rothman, J. Appl. Phys., 76, 5616 (1994)

[46] F. Faupel and T. Hehenkamp, Z. Metallkd. 84, 529 (1993)

[47] N. Chen, S.J. Rothman, J.L. Routbort, and K.C. Goretta, J. Mater. Res., 7, 2308 (1992)

[48] J. W. Ekin, Adv. Ceramic Mater., 2, 586 (1987)

[49] D. Dimos, P. Chaudhri, and J. Mannhart, Phys. Review B41, 4038 (1990)

[50] D. C. Larbalestier, Physics Today, 44, 74 (1991)

[51] J. R. Clem, Physica C153-155, 56 (1988)

[52] D. R. Clarke, T. M. Shaw, and D. Dimos, J. American Ceramic Soc., 72, 1103 (1989)

[53] S. E. Babcock and D. C. Larbalestier, Appl. Phys. Lett, 55, 393 (1989)

[54] M. F. Chisholm and S. J. Pennycook, Nature, 351, 47 (1991)

[55] P. Chaudhri, Physica C185-189, 292 (1991)

[56] M.kawasaki, P. A. Gupta, Phys. Rev. Lett., 68, 1065 (1992)

[57] S. E. Babcock, X. Y. Cai, D. L. Kaiser, and D. C. Larbalestier, Nature, 347, 6289 (1990)

[58] S. E. Babcock, MRS Bulletin, 17, 20 (1992)

[59] C. B. Eom, A. F. Marshall, Y. Susuki, B. boyer, R. F. Pease, and T. H. Geballe, Nature, 353, 544 (1991)

[60] S. E. Babcock and D. C. Larbalestier, J. Mater. Res., 5, 919 (1990)

[61] Y. Iijima, N, Tanabe, O. Kohno, and Y. Ikeno, Appl. Phys. Lett, 60, 769 (1992)

[62] X.D. Wu, S.R. Foltyn, P.N. Arendt, R.W. Blumenthal, I.H. Campbell, J.D. Cotton, J.Y. Coulter, W.L. Hultz, M.P. Maley, H.F. Safar, and J.L. Smith, Appl. Phys. Lett., 67, 2397 (1995)

[63] J.D. Budai, R.T. Yong, and B.S. Chao, Appl. Phys. Lett., 62, 1836 (1993)

[64] A. Goyal, D.P. Norton, J.D. Budai, M. Paranthaman, E.D. Specht, D.M. Groeger, D.K. Christen, Q.He, B. Saffian, F.A. List, D.F. Lee, P.M. Martin, C.E. Klabunde, E. Hartfield, and V.K Sikka, Appl. Phys.Lett., 69, 1795 (1996)

[65] J. E. Tkaczyk, C. L. Briant, J. A. Deluca, E. L. Hall, P. L. Karas, K. W. Lay, E. Narumi, and D. T. Shaw, J. Mater. Res., 7, 1317 (1992)

[66] D.E. Farrel, B.S. Chandrasekhar, M.R. DeGuire, M.M. Fang, V.G. Kogan, J.R. Clem, and D.K. Finnemore, Phys. Rev. B 36, 4025 (1987)

[67] R.H. Arendt, A.R. Gaddipati, M.F. Garbauskas, E.L. Hall, H.H. Hart, K.W. Lay, J.D. Livingston, F.E. Luborsky, and L.L. Schilling, in High Temp. Supercond., (eds. M.R. Brodsky, R.C. Dynes, K. Kitazawa, and H.L. Tuller), MRS, Pittsburgh, 1988, p203

[68] J.D. Livingston, H.H. Hart, and W.P. Wolf, J. Appl. Phys., 64, 5806 (1988)

[69] S. Jin and C. W, Chu, in Processing and Properties of High T_c Superconductors, Vol. 1, ed. S. Jin, World Scientific, Singapore, p431 (1993)

[70] C.P. Bean, Phys. Rev. Lett., 8, 250 (1962)

[71] E.M. Gyorgy, R.B.van Dover, K.A. Jackson, L.F. Schneemeyer, and J.V. Waszczak. Appl. Phys. Lett., 55, 283 (1989)

[72] Q. Qian, PhD thesis, Iowa State University, Ames, 1992, p36

[73] M. Tachiki and S. Takahashi, Solid State Comm., 70, 291 (1989)

[74] M. Tachiki and S. Takahashi, Solid State Comm., 72, 1083 (1989)

[75] M. Daeumling, J. M. Seuntjens and D. C Larbalestier, Nature, 346, 332 (1990)

[76] P. Groot, C. Beduz, Y-Zhu an, R. Yanru, and S. Smith, Physica C185-189, 2471 (1991)

[77] J. Mannhart, D. Auselmelti, J. g. Bednorz, C. H. Gerber, K. A. Muller, D. G. schlon, Proc. 6th Int. Workshop on Critical Currents in High T_c Supercond., Cambridge, UK, 5242 (1991)

[78] K. Salama, V. Selvamamckan, and D. F. Lee, in Processing and Properties of High T_c Superconductors, Vol. 1, ed. S. Jin, World Scientific, Singapore, p155 (1993)

[79] P.L. Doussal and D.R. Nelson, Physica C232, 69 (1994)

[80] J.W. Martin, Micromechanisms in Particle-hardened Alloys, Cambridge University Press, Cambridge, 1980, p21

[81] D. Porter and K. Easterling, Phase transformations in metals and alloys, 2nd. Ed. Chapman & Hall, London (1992) p263-313

[82] J.D. Verhoeven, Fundamentals of Physical Metallurgy, John Wiley & Sons, New York, 1975, p373-404

[83] H.I. Aaronson, J.K. Lee, and K.C. Russell, in Precipitation Process in Solids (eds. K.C. Russell and H.I. Aaronson), The metallurgical Soceity of AMIE, Warrendale, 1978, p31-86

[84] U. Balachandran, R.B. Poeppel, J.E. Emerson, S.A. Johnson, M.T. Lanagan, C.A. Youngdahl, D. Shi, and K.C. Goretta, Mater. Lett. 8, 454 (1989)

[85] T.B. Lindemer, F.A. Washburn, C.S. MacDougall, and O.B. Cavin, Physica C 174, 135 (1991)

[86] T.B. Lindemer, E.D. Specht, P.M. Martin, M.L. Flitcroft, Physica C 255, 65 (1995)

[87] H. Wu, M.J. Kramer, K. W. Dennis, and R.W. McCallum, Physica C, in press.

[88] M. Murakami, S.I. Yoo, T. Higuchi, N. Sakai, J. Weltz, N. Koshizuka, and S. Tanaka, Jpn. J. Appl. Phys. 33, L715 (1994)

[89] L. Li, PhD thesis, Ecole Polytechnique, Montreal, 1990

[90] T.B. Lindemer, E.D. Specht, C.S. MacDougall, G.M. Taylor, and S.L. Pye, Physica C 216, 99 (1993)

[91] M. Nakamura, H. Kutami, and Y. Shiohara, Physica C 260, 297 (1996)

[92] E.A. Goodilin, N,N, Oleynikov, E.V. Antipov, R.V. Shpanchenko, G. Yu. Popov, V.G. Balakirev, Yu.D. Tretyakov, Physica C 272, 65 (1996)

[93] M. Nakamura, Y. Yamada, T. Hirayama, Y. Ikuhara, Y. Shiohara, and S. Tanaka, Physica C 259, 295 (1996)

[94] G.F. Voronin and S.A. Degterov, J. Solid State Chem. 110, 50 (1994)

[95] H. Wu, M.J. Kramer, K. W. Dennis, and R.W. McCallum, Appl. Phys. Lett., in press.

[96] A. Ourmazd, J. A. Rentschler, J.C.H. Spence, M. O'Keeffe, R. J. Graham, D.W. Johnson Jr. and W.W. Rhodes, Nature (London) 327, 308 (1987)

[97] K. Kuroda, K. Abe, S. Segawa, J. Wen, H. Unoki, and N. Koshizuka, Physica C 275, 311 (1997)

[98] A.M. Hu, Z.X. Zhao, M.Z. Wu, C. Wende, T. Strasser, B. Jung, G. Bruchlos, W. Gavalek, and P. Goernert, Physica C 278, 34 (1997)

[99] T. Egi, J.G. Wen, K. Kuroda, H. Unoki, and N. Koshizuka, Appl. Phys. Lett., 67, 2406 (1995)

[100] T. Egi, J.G. Wen, K. Kuroda, H. Mori, H. Unoki, and N. Koshizuka, Physica C 270, 223 (1996)

[101] T.Higuchi, S.I Yoo, K. Sawada, N. Sakai, and M. Murakami, Physica C 263, 396 (1996)

[102] W. Ting, T. Egi, K. Kuroda, N. Koshizuka, and S. Tanaka, Appl. Phys. Lett., 70, 770 (1997)

[103] T. Hirayama, Y. Ikuhara, M. Nakamura, Y. Yamada, T. Hirayama, and Y. Shiohara, J. Mater. Res., 12, 293 (1997)

[104] L. Civale, T.K. Worthington, L. Krusin-Elbaum, A.D. Marwick, F. Holtzberg, J.R. Thopmson, M.A. Kirk, and R. Wheeler, JOM, 44, 60 (1992)

ACKNOWLEDGMENTS

I would like to thank Dr. R.W. McCallum for the opportunity to do research in this fascinating field of high temperature superconductivity. I would like to thank him for his guidance and patience. I would like to thank Dr. M.J. Kramer for his assistance in TEM, which giving much insight into the precipitation mechanism. I am also grateful to Mr. K.W. Dennis for his invaluable technical assistance. I would like to thank L. Margulies, C.P. Li, M. Park, S.I. Yoo, D. Branagan, C. Schwichtenberg, and A. O'Connor for many helpful discussions.

I would like to thank Dr. R.K. Trivedi, Dr. J.D. Verhoeven, Dr. D. K. Finnemore, Dr. A. I. Goldman, and Dr. P. C. Canfield for their time and effort spent on my graduate committee.

This work was performed at Ames Laboratory under contract No. W-7405-eng-82 with the U.S. Department of Energy. The United States Government has assigned the DOE Report Number IS-T 1834 to this thesis.

Report Number (14) IS-T--1834

Publ. Date (11) 19980223

Sponsor Code (18) DOE/ER, XF

UC Category (19) UC-400, DOE/ER

DOE